

1 **The interplay between bi-modal molecular weight distribution polystyrene/methyl ethyl**
2 **ketone solution and humidity induces self-assembly of islands/honeycomb structure in the**
3 **thin polymer film**

4 Authors: Maciej Łojkowski^{1,*}, Adrian Chlanda^{1,2}, Emilia Choińska¹, Wojciech
5 Swieszkowski^{1,*}.

6

7 Affiliation:

8 1. Faculty of Material Sciences and Engineering, Warsaw University of Technology,
9 Wołoska 141, 02-507 Warsaw, Poland

10 2. Department of Chemical Synthesis and Flake Graphene, Łukasiewicz Research
11 Network - Institute of Microelectronics and Photonics, Aleja Lotników 32/46, 02-
12 668 Warsaw, Poland.

13 **Abstract**

14 Segregation of polymer chains of different molecular weights is a well-known process. A
15 traditional experimental approach of studying phase segregation in thin films composed of
16 polymer blends with identical chemical compositions but different molecular weights was
17 focused on functionalizing chemical groups or modifying end groups. In this study, however, a
18 different approach was proposed. Polystyrene with bimodal molecular weight distribution, but
19 no additional chemical modification was used. The films were prepared by spin-coating, and
20 the segregation between polystyrene phases was investigated by force spectroscopy. The
21 solubility of bimodal polystyrene was explored. At the proper molecular weight distribution
22 and soluted in methyl ethyl ketone, phase separation occurred. The introduction of moist airflow
23 induced the secondary phase separation of the lower molecular weight into islands and the
24 heavier fraction self-organized into a honeycomb. As a result, an easy, fast, and effective

25 method of obtaining island/honeycomb morphologies was demonstrated. The possible
26 mechanisms of the formation of such structures were discussed.

27

28 **Keywords**

29 self-assembly; polymer thin films; bimodal molecular weight distribution; polystyrene; spin-
30 coating; honeycomb; breath figures; liquid-liquid phase separation; viscoelastic phase
31 separation; secondary quench;

32

33 **Introduction**

34 Complex morphologies comprising micro-islands and especially micropillars have gained
35 attention due to their wide range of possible applications, such as their special wetting
36 properties (1,2), application in studying biofilm formation (3), or controlling stem cell
37 differentiation (4). Two widespread methods that allow the creation of a broad range of
38 structures of polymer thin films (PTFs) are spin-coating (5) and breath figures (6). These
39 methods were applied for manufacturing organic ferroelectric switches (7), light-emitting
40 devices (8), sensors (9,10), drug delivery systems (11,12), biologically active surfaces (13,14),
41 functional nanostructured surfaces (15,16), and membranes (17). These processes rely heavily
42 on the interaction dynamics between the solvent, the polymer, and the vapours in the vicinity
43 of the surface. During spin-coating, a droplet of a mixture of a solvent and one or two polymers
44 is dropped onto the substrate. Subsequently, the substrate is rotated very quickly to cover it
45 uniformly with the solution's liquid film. As a result, the solvent evaporates. Thus, solvent and
46 temperature quench occurs. The spin coating can be divided into time regions. At first, the
47 liquid solution's droplet is spread hydrodynamically over the substrate. This regime is often
48 referred as hydrodynamic thinning. Later on, when a flat layer of the solution has obtained, the
49 evaporation of the solvent is responsible for further thinning of this layer.(18) Changes in the

50 solvent volume fraction and temperature often lead to unintentional or intentional liquid-liquid
51 phase separation.(19) It has been argued that such phase separation often starts in the early
52 stages of the regime controlled by evaporation.(19,20) Further spinning of the solution leads to
53 gel formation, which eventually slows down the diffusion inside the film. As a result, the
54 morphology becomes frozen in time before reaching equilibrium. The time necessary for the
55 morphology to stop evolving depended on the solvent evaporation rate, solution viscosity,
56 spinning rate, and substrate thermal properties.(21–23) During coating formation range of
57 events attributed to the local thermal instabilities takes place: heat transfer between the bottom
58 and the top layers of the film; heat transfer from the air above the layer; heating the substrate
59 by the surrounding air; local lateral temperature variance, due to the thermal conductivity and
60 heat capacity of the substrate.(23) These events may lead to the unnecessary or intended
61 waviness of the coating profile. This undulation is often attributed to two interconnected
62 phenomena. One is the flow of the liquid due to the thermal convection. The second is the
63 surface tension gradient due to local composition differences, which manifests in solvent-rich
64 or solvent-depleted areas.(18) The solvent-depleted areas have higher surface tension, thus,
65 pulls the liquid towards these areas and up, while the solvent-rich areas sink, forming valleys.
66 High centrifugal force during spin-coating is often a cause of elongation of the mentioned
67 structures. As a result, long stripes extending from the centre of the sample are observed. Using
68 solvent with low surface tension, the addition of a surfactant or using a mixture of solvents can
69 suppress the formation of these features. Furthermore, decreasing the amount of heat can
70 suppress the formation of the convection cells and allow smooth coating preparation.

71 In the second technique mentioned above, breath figures appear on the liquid film's surface
72 when the humid airflow accelerates the evaporation rate. Successively, the temperature
73 decreases, which results in nucleation and growth of water droplets. These droplets create a
74 regular honeycomb array of cavities in the film. The temperature increased to that of the

75 surroundings, and the droplets evaporated, leaving a porous surface, after most of the solvent
76 had evaporated, The start of droplet nucleation is governed by the onset time related to the
77 solvent evaporation rate, solution concentration, and airflow.(24)

78 The location and width of the MWD can affect, solid thin polymeric film formation to achieve
79 unique properties (25). Wu et al. studied the effect of MWD on the self-assembly of end-
80 functionalized polystyrenes. They proposed a new way of controlling the morphology of PTF
81 obtained via breath figures by changing the MWD width. As a result, a porous membrane with
82 higher robustness was obtained.(26) The width of the MWD can be tailored either within the
83 polymerization process (27,28) or by mixing two polymer species with a very narrow MWD
84 (29). Heitmiller et al. reported a heterogeneous melt of polyethylene had a higher flow index
85 than a homogeneous melt.(30) The investigation performed by Koningsveld et al. has shown
86 that the bimodal MWD has a significant effect on the liquid-liquid binodal curve of polymers
87 in solution.(31) Phase regions characterise such solutions, and liquid-liquid phase separation
88 between polymer- and solvent-rich fractions can occur. Zeman et al. demonstrated that the
89 critical concentration enabling phase separation in a solution of two polymer species decreases
90 with an increase in the molecular weight M_w .(32) Moreover, even when the polymer-polymer
91 interactions are athermal, i.e. the Flory-Huggins interaction parameter χ equals zero, and phase
92 separation can occur due to the large difference in entropy between long and short chains, which
93 act as separate entities and influence the viscosity of bimodal solutions.(33) The evaporation of
94 the solvent followed by temperature quench can be responsible for phase separation as the
95 Flory-Huggins parameter is temperature dependant and decreases with temperature. The
96 quenched mixture can turn from the one phase state to an unstable state. Interestingly,
97 Henderson et al. have investigated a two-step process where the first temperature quench forces
98 the phase separation, and the spinodal structures are allowed to coarsen, next, even deeper
99 quench is enacted.(34) This two-step quench led to the formation of small well-dispersed

100 domains within the primary domains. Intriguingly, the combined spin-coating and breath figure
101 methods would lead to two quench and heating events. First, the solvent evaporation would
102 decrease temperature. Secondly, the water condensation would increase the temperature, and
103 finally, the evaporating water would again decrease the temperature. Another interesting theory
104 is the “viscoelastic phase separation”. There, the phase separation occurs due to an imbalance
105 of the viscoelastic properties of the components.(35) Polymer melt with bi-modal molecular
106 weight shows non-linear rheology. A rheological investigation by Hengeller et al. has reported
107 two regimes of stress relaxation in such melt, where either the only short or only long chains
108 underwent stress relaxation, depending on the time scale.(36) Harris et al. found that the
109 viscosity of the blend of bimodal polystyrene can be considered a sum of components.(37) It
110 has been discussed that blending polystyrenes with different molecular weights mixed the
111 entanglement types between polymer chains. The polymer concentration in the solvent changes
112 how the polymer chains interact. Two polymer chains act as separate entities, provided that the
113 concentration is below the overlap concentration (C^*). However, once the overlap
114 concentration occurs, the polymer's cooperative motion starts, and the behaviour of the solution
115 changes.(38,39)

116 Successive research has focused on studying how polymer chains of varying lengths segregate
117 in PTFs. Hariharan et al. investigated the effect of the entropy of spin-coated and annealed
118 bimodal PTFs on polymer chain segregation.(40) It was shown that higher entropy of shorter
119 chains led to their segregation on the PTF surface, while the longer chains' lower entropy
120 promoted their segregation in bulk. Tanaka et al., in turn, studied spin-coated polystyrene
121 blends with low and high M_w with narrow MWD utilizing toluene as a solvent. They reported
122 that PTFs consisting of polystyrenes with a low molecular weight demonstrated surface
123 segregation after thermal treatment.(29) Several other recent studies have illustrated the
124 segregation of lower molecular mass elements towards the surface during annealing.(41–45)

125 On the other hand, it has been shown that deuterated polymer segregation can change the
126 surface roughness after annealing the coating.(46–49)

127 In the present study, to modify the coating's morphology, we decided to explore the phase
128 separation between two kinds of polystyrene, with low and high molecular weight, mixed in a
129 solvent. We changed the polydispersity, and we used uniform polystyrene standards as a
130 reference. The solvent, methyl ethyl ketone, MEK, was chosen because its suitability for spin-
131 coating.(50) But for most, its hygroscopic properties as we planned to perform spin-coating in
132 humid conditions. MEK is considered a marginal solvent for PS, while it is more hygroscopic
133 than typically used solvents for polystyrene.(51,52)

134 For our study, we established the following assumptions. The mixture with high enough
135 polydispersity will phase separate during spin-coating, even if these species are chemically
136 identical. The study will be performed in the regime where thermocapillary effects cause
137 undulations to make any morphological changes clearer to observe. The breath figures
138 technique will be combined with the spin-coating to induce additional motion caused by the
139 surface tension of water.

140 The study is organized in the following order. First, the effect of bi-modal weight distribution
141 on the viscosity of the solutions is discussed. Next, the morphology of the coatings spun at the
142 most negligible possible humidity is compared by analysis of atomic force microscopy and
143 optical microscopy images. Then, force spectroscopy was used to identify the different
144 polystyrene phases. The in-situ reflectometry was used to measure the evaporation time of the
145 solutions. Finally, the coatings spun at different humidity levels were investigated by optical
146 and atomic force microscopy.

147 It was found that at a relative humidity of 75%, solution concentration 80 mg/ml and
148 polystyrene molecular weights 20 kDa and 200 kDa mixed in 75/25 w/w% ratio the two phases
149 forms island (lower M_w fraction) embedded inside of the honeycomb (higher M_w fraction).

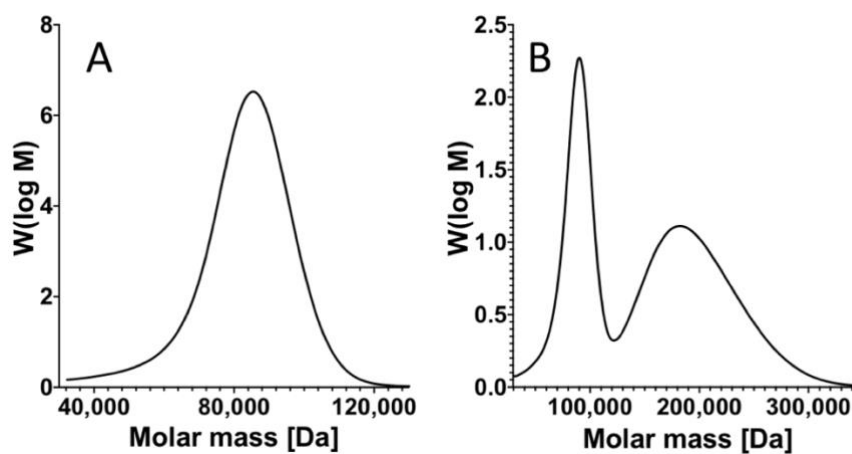
150 Although spin-coating was chosen for its ease of controlling the evaporation rate, we believe
151 that the proposed method can be extended to other techniques, such as dip-coating or ink-jet
152 printing. Presented results can also be treated as a starting point for other interesting
153 experiments.

154

155 **Result and discussion**

156 The solutions with bimodal MWD were prepared so that the two nodes in the distribution were
157 clearly separated. The GPC molecular weight distribution of a single node MWD (uniform) is
158 presented in Fig. 1 A, which illustrates the MWD of 91 kDa polystyrene with a narrow
159 distribution (PDI=1.04). In contrast, Fig. 1 B illustrates the MWD with two nodes of a blend of
160 91 kDa PS with 200 kDa PS, both with narrow distributions (PDI=1.04).

161



162

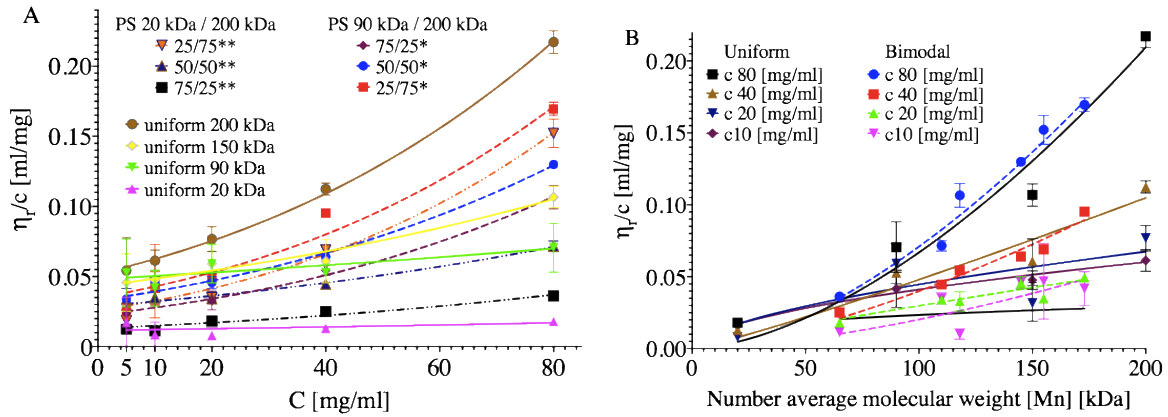
163 Fig 1. Exemplary GPC experiment results of bimodal and uniform MWD polystyrene; A -
164 narrow uniform MWD, $M_w = 91$ kDa, PDI 1.04; B – bimodal MWD, blend of $M_w = 91$ kDa,
165 PDI = 1.04 and $M_w = 200$ kDa, PDI = 1.04.

166

167 • **Evaluation of solution viscosities**

168 The viscosity measurement (Fig. 2) can be used to assess not only the final coating thickness
169 and the solvent evaporation time prediction but also the characteristics of polymer chain

170 interactions. The measurement result is presented as reduced viscosity η_r/C , where C represents
 171 the concentration in mg/ml. Here, $\eta_r = \frac{\eta - \eta_s}{\eta_s}$, where η is the dynamic viscosity of the solution
 172 and η_s is the viscosity of the solvent. In Fig. 2A, the viscosity is plotted as a function of the
 173 concentration.
 174



175
 176 Fig. 2. Reduced viscosity η_r/C of the solutions, A - η_r/C plotted against the solution's
 177 concentration. Curves represent fits for eq. 2; B - η_r/C plotted as a function of the number
 178 average molecular weight function. Curves represent the Mark-Houwink equation fit (eq. 3),
 179 $[M_n] = f_1M_{w1} + f_2M_{w2}$, where f is w/w % ratio of polymers.

180
 181 The general dependence of viscosity on concentration can be described in the form of a power
 182 series:(53)

$$183 \frac{\eta_r}{c} = [\eta] \left(1 + K[\eta]C + \frac{K[\eta]C^2}{2} + \frac{K[\eta]C^3}{6} \right) \quad (2)$$

184 where $[\eta]$ is the intrinsic viscosity at infinite dilution. The coefficients are summarised in Table
 185 S1 in SI. The intrinsic viscosity $[\eta]$ was lower for bimodal blends. The overlap concentration is
 186 defined as a concentration at which the polymer chains start to overlap each other.(54) The
 187 overlap concentration was estimated according to $C^*=1/[\eta]$. The overlap concentration for 20
 188 kDa was 83 mg/ml and for 200 kDa was 19 mg/ml. As it should be noticed, in the case of the

189 80 mg/ml solution, the 20 kDa species were in the semi-dilute regime, while the 200 kDa were
 190 in the concentrated regime.

191 The viscosity of the bimodal solutions increased faster with increasing concentration than in
 192 the case of uniform solutions. The K parameter was particularly high for 75/25 blends: 1.36 for
 193 90 kDa and 200 kDa and 1.01 for 20 kDa and 200 kDa. In comparison, K for uniform 200 kDa
 194 was 0.36. Thus, it can be assumed that the number of entanglements attributed to the 200 kDa
 195 fraction rises at higher concentrations. Fig. 2B presents the viscosity in relation to the number
 196 molecular weight $[M_n]$. The relation between viscosity and molecular weight can be described
 197 in the form of the Mark-Houwink equation:(53)

$$198 \frac{\eta_r}{c} = \ln K + a \ln[M_n]. \quad (3)$$

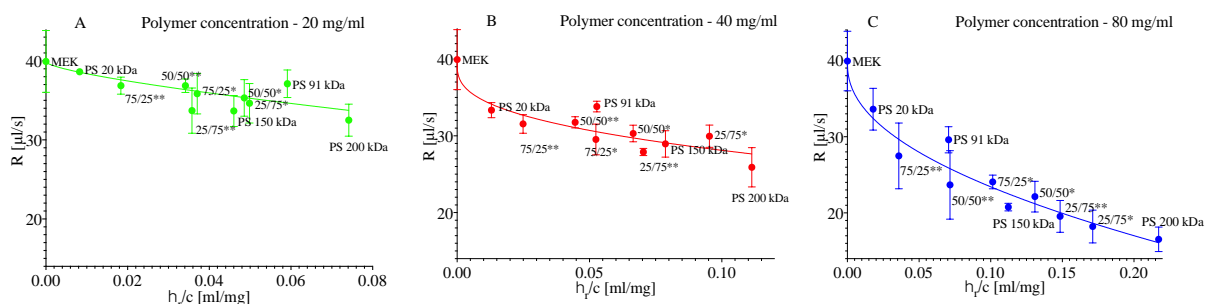
199 The K and $[\eta]$ values are summarised in SI, Table S2. The uniform solutions were visibly more
 200 viscous than their bimodal counterparts of similar molecular weights at concentrations below
 201 20 mg/ml. It could be expected that the bimodal solutions will change their behaviour more
 202 severely when solvent's evaporation would quench them towards more concentrated regimes.

203

204 • **Evaporation of the solvent during spin-coating**

205 As presented in Fig. 3, the evaporation rate R depends on the viscosity of the solutions. It can
 206 be noticed that the evaporation of the 20 kDa, 91 kDa and 200 kDa differ for the same
 207 concentration. These differences become more transparent for the concentration of 80 mg/ml.

208



209

210 Fig. 3. The relation between the evaporation rate of solution and the reduced viscosity of
211 solution for polymer concentrations: A - 20 mg/ml, B - 40 mg/ml, and C - 80 mg/ml. The curves
212 represent the Padé approximation trend-line.

213

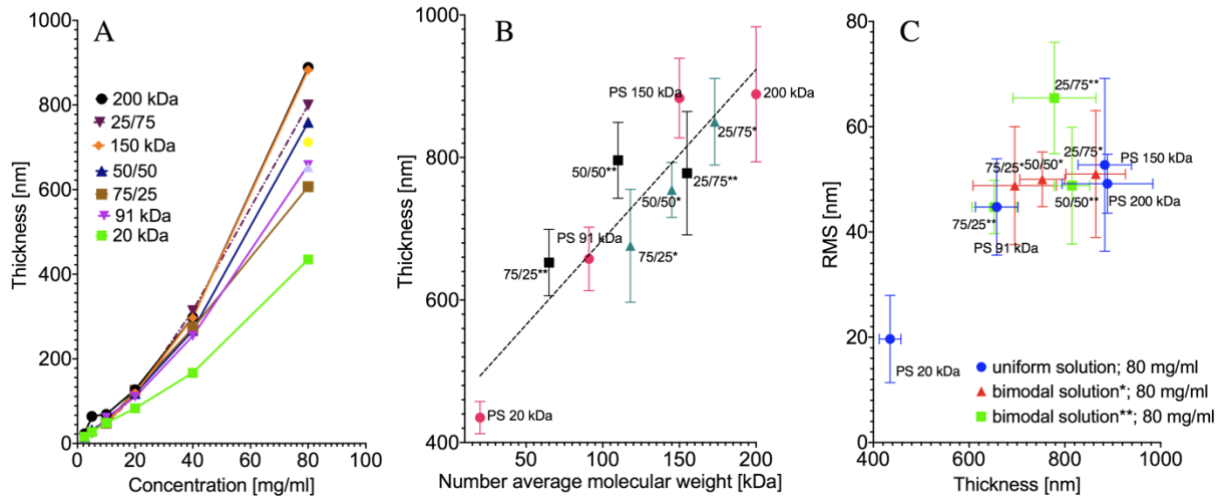
214 • **Investigation of the thickness and morphology of the coatings spun at a relative**
215 **humidity of 0%**

216 The coatings spun at Rh 0% were chosen as a starting point for the investigation. We decided
217 to look for phase separation if no humidity was applied, affecting the investigated solvent-
218 polymer system. The convection Marangoni flow, solvent evaporation, and phase separation
219 events alter the coating surface morphology. As a result, the occurrence of wrinkles or arrays
220 of islands on the coating surface was reported. (48,55–57)

221 The coatings were investigated via AFM and optical imaging to determine the effect of bimodal
222 MWD on coating morphology. Significant differences between blend types occurred (Fig. 4A).

223 The solution concentration of 80 mg/ml was chosen. As we expected from the tests as
224 mentioned earlier, the bimodal distribution role would be the highest. Moreover, we wanted to
225 avoid the influence of the substrate on our force spectroscopy experiment. For that, we needed
226 the thickest coating. As illustrated in Fig. 4B, the thickness of the coatings in the case of 80
227 mg/ml scaled linearly with the blends' average molecular weight. No correlation between the
228 thickness and roughness was found. (Fig. 4C).

229



230

231 Fig. 4. A - Thickness of the coatings with respect to the composition and the concentration. The
 232 plot presents data for uniform and 91 kDa/200 kDa solutions. B – Thickness of the coating for
 233 80 mg/ml concentration in the blend's molecular weight function. * - Blends of 91 kDa and 200
 234 kDa polystyrene; ** - blend of 20 kDa and 200 kDa polystyrene; x/x – w/w% ratio of blended
 235 homogeneous polystyrenes. The number average molecular weight $[M_n] = f_1M_{w1} + f_2M_{w2}$,
 236 where f w/w. % ratio of polymers. C - RMS roughness of the coatings spun from 80 mg/ml
 237 concentration.

238

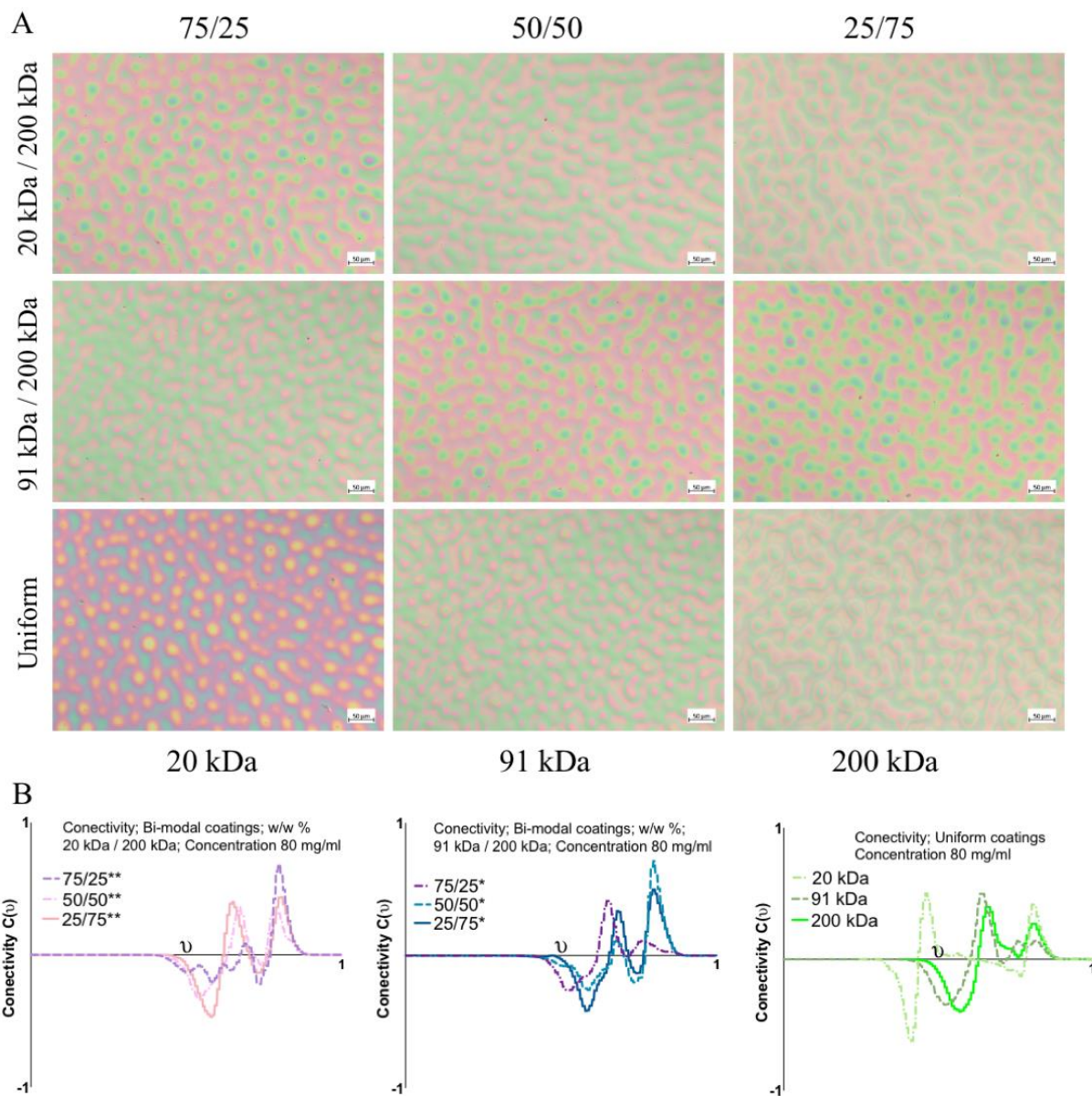
239 To represent the morphology of the material quantitatively, one can apply the Minkowski
 240 parameters.(58) The images (Fig. 5A) used for analysis come from the central part of the image
 241 to exclude the high shear rate effect on the coating morphology. The scale bar was 50 μ m.
 242 Based on this description, it can be concluded that the morphology of the uniform coatings is
 243 characterised by separate islands surrounded by a bicontinuous phase. In contrast, the bimodal
 244 coatings are characterised by a bicontinuous phase, separated by interconnected islands.

245 Fig. 5B presents connectivity. Connectivity $C(\nu)$ can be used to describe the bicontinuous or
 246 island morphology of the coating with respect to the given binarization threshold ν . The
 247 negative value of connectivity corresponds to bicontinuous morphology, while the positive
 248 value corresponds to island morphology. The threshold was normalized to 1. Basing on the

249 connectivity, it can be shown that the bimodal coatings had different morphologies than the
250 uniform coatings when the starting conditions (Rh 0%) were considered. With the exclusion of
251 75/25 20 kDa 200 kDa coating, the coatings were characterized by peaks related to continuous
252 structures and two peaks related to islands.

253 On the contrary, the uniform coatings had one set of continuous structure and two peaks related
254 to islands. In connection with the images, it can be assumed that these two kinds of islands are
255 one on top of another. In the case of bimodal blends, the presented situation describes a set of
256 interconnected islands on top of another interconnected structure.

257



258

259 Fig. 5. A - Optical images of coatings spun from 80 mg/ml. The B - Minkowski connectivity

260 $C(\nu)$ of the coatings spun from 80 mg/ml, where ν represents the threshold for the image

261 binarization; The values on the axis were normalized to 1.

262

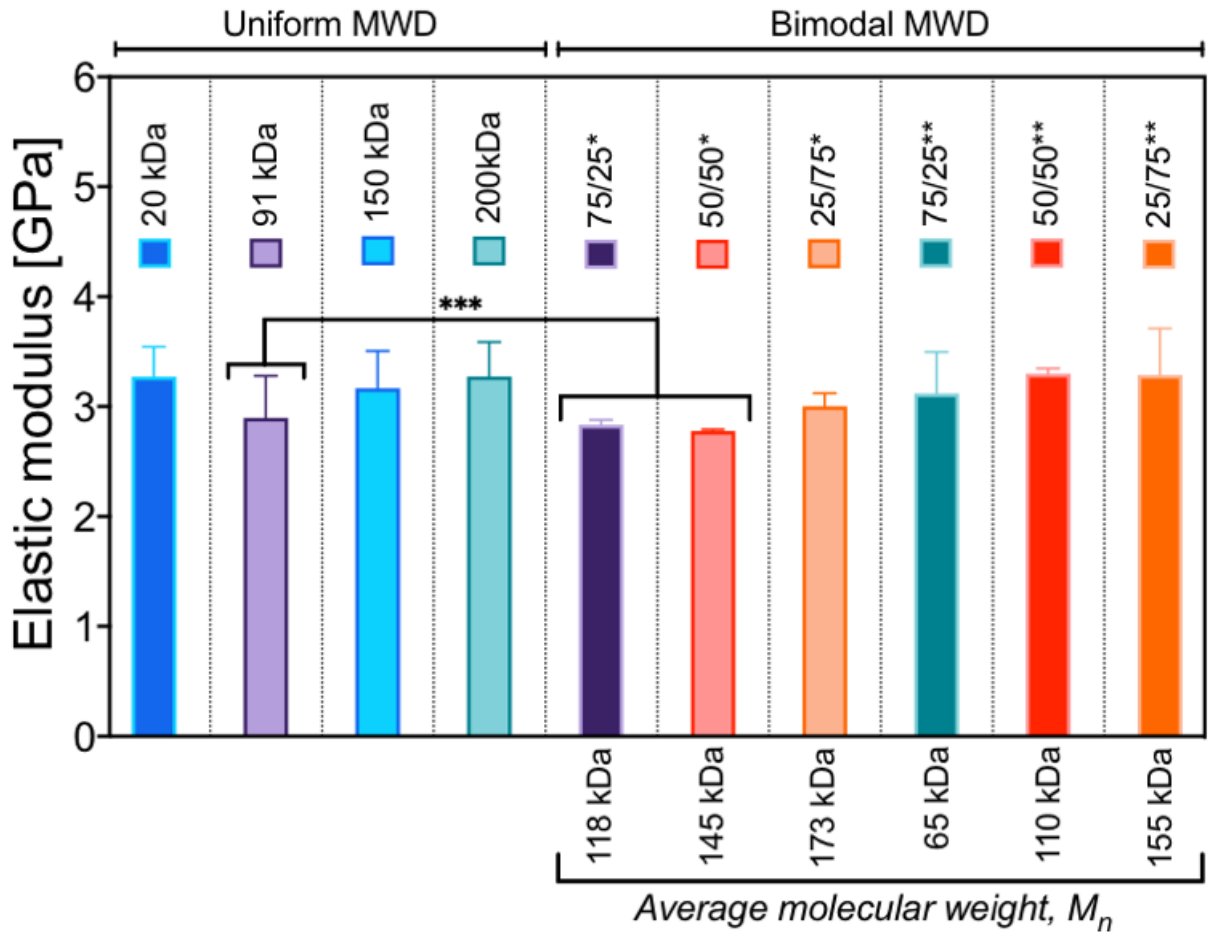
263 • **Investigation of coating phase composition by means of AFM force spectroscopy**

264 The AFM force spectroscopy method allows the visualization and quantification of surface

265 areas differing in mechanical properties.(59) The coatings spun from the solutions with 80

266 mg/ml concentration were studied. The resulting elastic modulus of the coatings was calculated
 267 (Fig. 6).

268



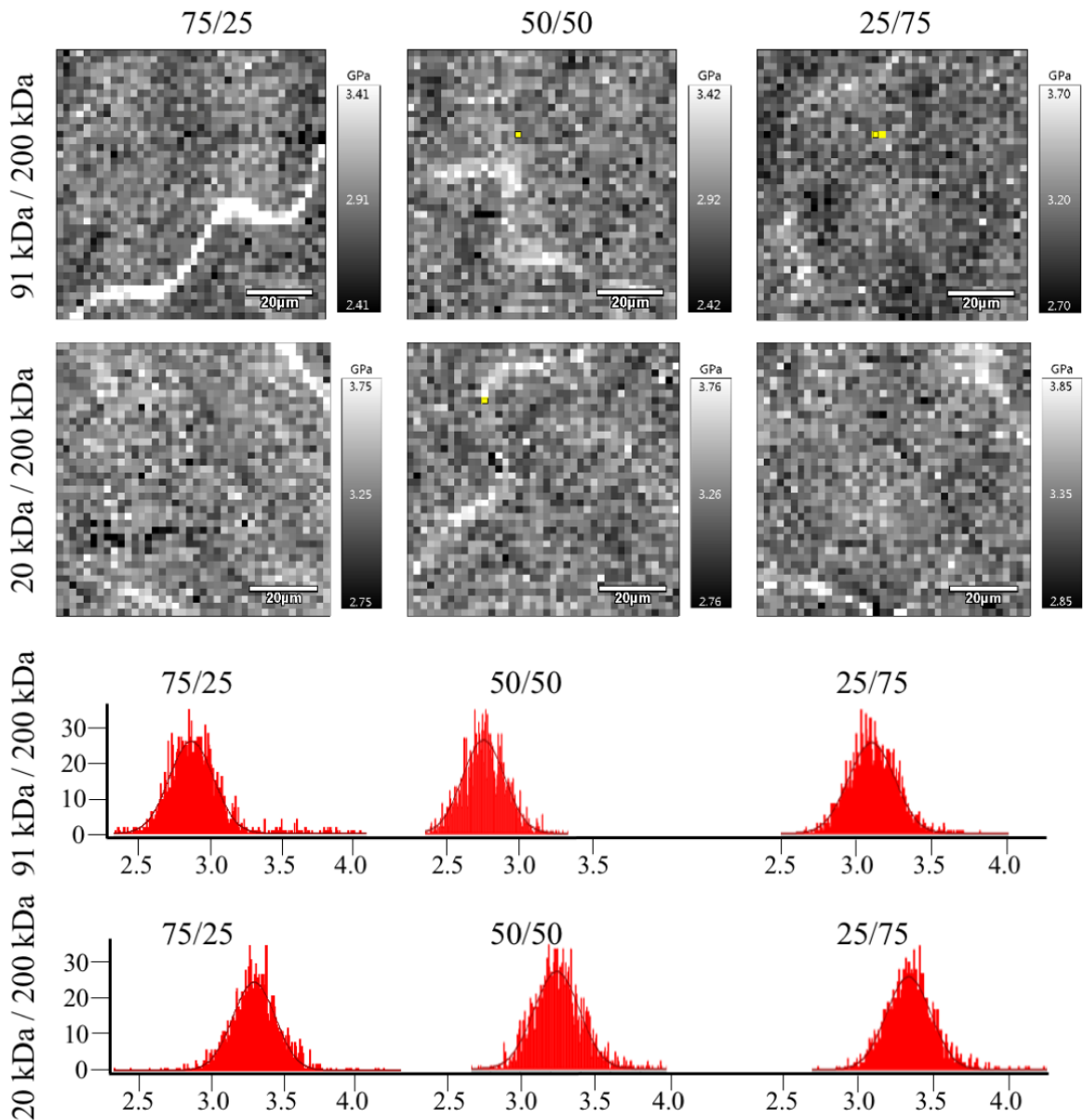
269

270 Fig. 6. Average elastic modulus obtained based on the FS method for coatings made from a
 271 solution of 80 mg/ml. Uniform – coatings were made from homogeneous solutions; bimodal –
 272 coatings made from solutions with bimodal MWD; * - blends of 91 kDa and 200 kDa
 273 polystyrene; ** - blend of 20 kDa and 200 kDa polystyrene; x/x – w/w% ratio of blended
 274 homogeneous polystyrenes. $[M_n] = f_1M_{w1} + f_2M_{w2}$, where f w/w % ratio of polymers. *** -
 275 means are significantly different (one-way ANOVA, $p < 0.05$).

276

277 The obtained results are similar to those found in the literature.(60) The uniform 91 kDa coating
 278 and the 75/25 and 50/50 blends of 91 kDa and 200 kDa had significantly lower elastic moduli

279 than the rest of the tested groups. The dependence between the molecular weight and the elastic
280 modulus of the polymer has been repeatedly proven.(61,62) However, we did not find
281 significant differences between the other groups. The uniform 20 kDa coating had an elastic
282 modulus similar to that of the 200 kDa coating in our investigation. The 20 kDa coating was
283 the thinnest; thus, the substrate could influence the result. We performed a linear regression test
284 (SI, *Force Spectroscopy*, Fig. S4) between the thickness of the 80 mg/ml coatings and the elastic
285 modulus, which proved no relationship between the thickness of the coatings and the elastic
286 modulus, while the 20 kDa coating was an outlier (SI, *Force Spectroscopy*, Table 14).



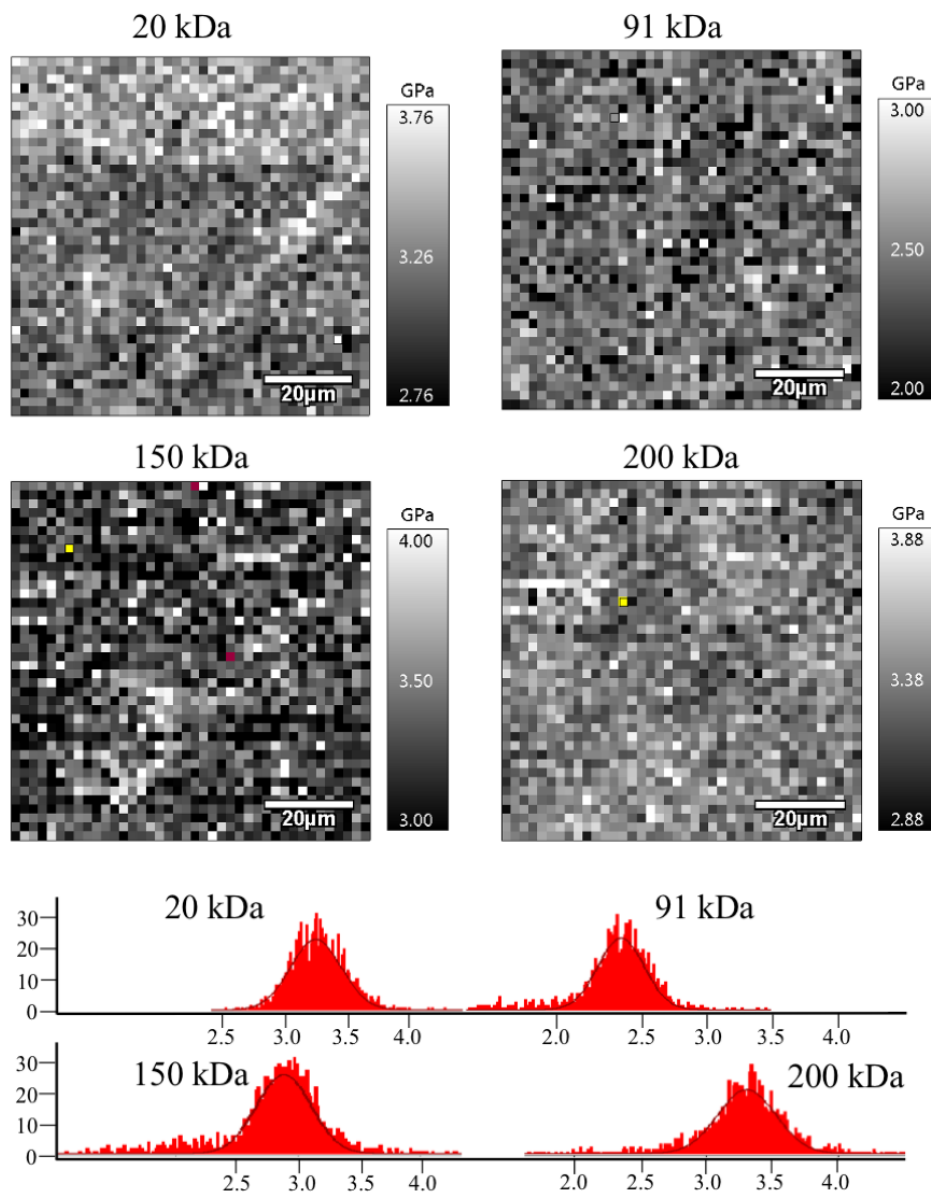
287

288 Fig. 7. Force Spectroscopy maps of bimodal MWD coatings and corresponding histograms of
289 the elastic modulus. The greyscale shows the stiffness – the white colour corresponds to the
290 highest stiffness. The grayscale range is ± 1 GPa.

291

292 Interestingly, it was possible to record local differences in the coating surface stiffness (Fig. 7).
293 The maps were gathered for bimodal coatings. White spinodal-like areas are characterized by
294 higher stiffness. The differences are more clearly visible in the case of 90 kDa and 200 kDa
295 blends, in agreement with Fig. 6.

296



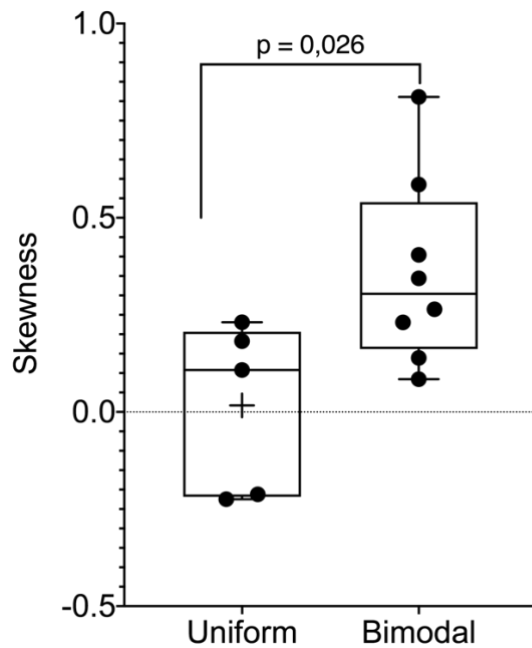
297

298 Fig. 8. Force spectroscopy maps of coatings with uniform MWD and corresponding histograms
 299 of the elastic modulus. The greyscale shows the stiffness – the white colour corresponds to the
 300 highest stiffness. The grayscale range is ± 1 GPa.

301

302 For comparison, Fig. 8 illustrates the FS maps of the uniform coatings. We analysed the
 303 skewness of the maps' elastic modulus distribution (SI, *Force Spectroscopy*, Table S15). The
 304 skewness in the case of uniform coatings was significantly lower ($p < 0.05$) than that in the case

305 of bimodal coatings (Fig. 9). The distribution of the elastic modulus of the uniform coatings
306 was more homogeneous.



307
308 Fig 9. The skewness of the elastic modulus data sets. Uniform – grouped means that represents
309 the skewness of histograms of uniform coatings elastic modulus. Bimodal – grouped means that
310 represents the skewness of histograms of all kinds of bimodal blends elastic modulus. The
311 means of these two groups were significantly different ($p < 0.05$).

312
313 Therefore, it was concluded that force spectroscopy revealed the phase separation in the
314 bimodal coatings. The most noteworthy phase separation was found for the 75/25 blends of
315 both kinds of bimodal coatings. Here, the phase of lower concentration formed long, spinodal-
316 like forms. For the 25/75 blends, the separate phases were scattered.

317
318 • **Solubility of polystyrenes with respect to the molecular weight distribution**

319 The phase separation as mentioned above could be explained by solubility investigation. It was
320 shown that the viscosity of the polymeric solution could be utilised by the application of the
321 Mangaraj method to retract several polymer-solvent parameters, i.e. the Flory interaction

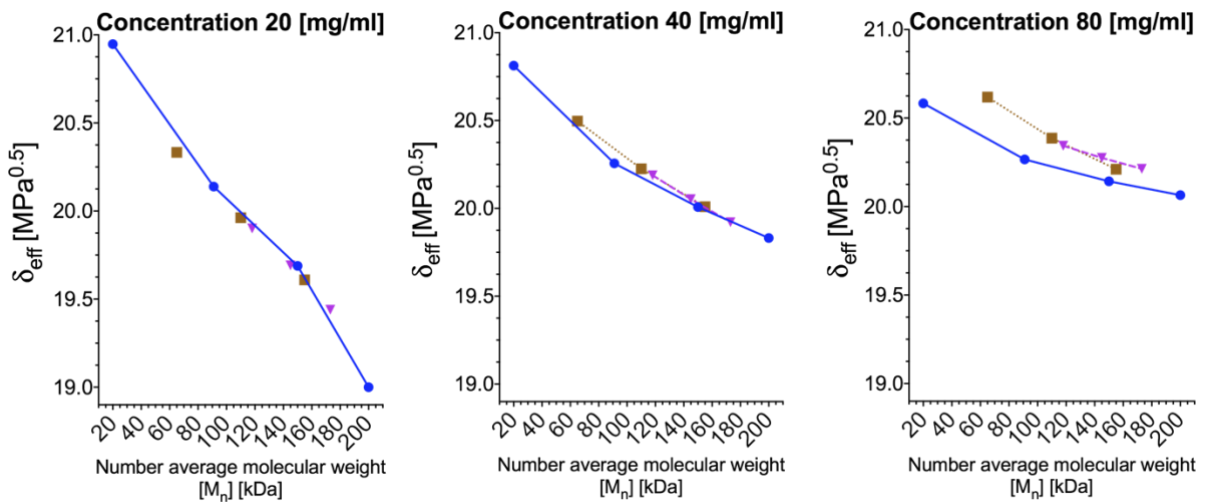
322 parameter.(63) We utilised the Mangaraj equation (eq. 4) to investigate the miscibility gap
 323 between the lower- and higher-molecular-weight polystyrenes.(64)

$$324 \ln\left(\frac{\eta}{\eta_{max}}\right) = -(\delta_s - \delta_{eff})^2. \quad (4)$$

325 The effective miscibility parameter δ_{eff} was calculated with respect to a solution of 200 kDa
 326 with a concentration of 80 mg/ml, which had the highest viscosity among the tested solutions
 327 (η_{max}). The solvent δ_s was set to 19 MPa^{0.5}, which is a typical value for MEK.

328 The miscibility gap between low- and high-molecular-weight polystyrene can be derived based
 329 on the PS blends' viscosity. Furthermore, the miscibility gap decreases accordingly with the
 330 low molecular weight fraction. Here, δ_{eff} is the effective Hildebrand miscibility parameter
 331 calculated based on the intrinsic viscosity $[\eta]$. For the 20 mg/ml concentration, all the solutions
 332 are present on the same linear trend with the lowest δ_{eff} for the highest molecular weight. It
 333 should be noted that with increasing concentration, the trends for 20 kDa/200 kDa solutions
 334 (brown squares), 91 kDa/200 kDa solutions (purple triangles), and uniform solutions (blue
 335 circles) become divergent at low molecular weights, with their trends coincident at 200 kDa
 336 (Fig. 10).

337



338

339 Fig. 10. The effective miscibility parameter δ_{eff} of the polystyrenes in MEK with bimodal and
340 uniform distributions for two kinds of bimodal distributions: 20 kDa/200 kDa – brown squares
341 and 91 kDa/200 kDa – purple triangles; the blue circles represent data for polystyrenes with
342 uniform distributions. $[M_n] = f_1M_{w1} + f_2M_{w2}$, where f w/w % ratio of polymers.

343

344 • **Self-assembly of micro islands/honeycombs due to phase separation and water**
345 **condensation**

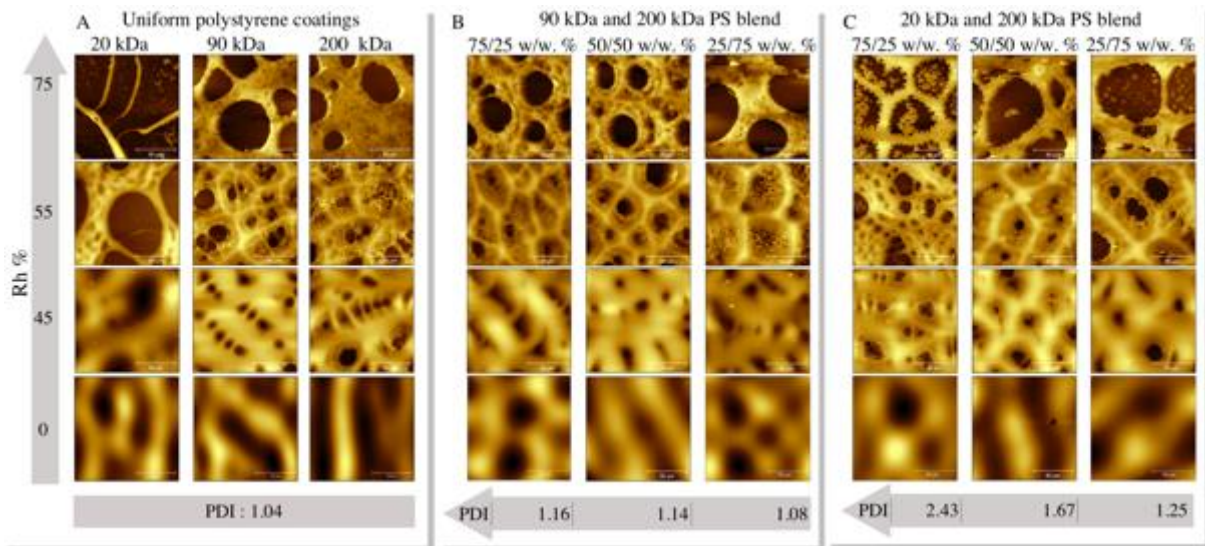
346 As a follow-up, we utilized humidity to take advantage of the phase separation observed above.
347 It was assumed that phase separation could be further enhanced if spin-coating was performed
348 under humid conditions. It was further concluded that water condensation would eventually
349 lead to ruptures in the solution layer. By this, a new interface between the solution, water, and
350 SiO₂ substrate would be created. This would induce separation between segregated phases. The
351 condensing water forces the liquid film to dewet and retreat from SiO₂. The viscosity gradient
352 between different phases would lead to the formation of convection cells and honeycomb
353 morphology.(65,66) It was assumed that the spinodal-like structures found during the FS
354 investigation, probably consisting of a higher molecular weight fraction, would reinforce the
355 honeycomb borders. As was revealed by the viscosity investigation, the longer polymer chains
356 would carry the stress as they would be highly entangled. The lower molecular phase would
357 separate because no stress would be applied to the shorter chains. It should also be considered
358 that MEK is a hygroscopic solvent, while PS is slightly hydrophobic. The absorption of water
359 by MEK can further alter the interactions between the solvent and different PS phases. The
360 viscosity and solubility investigations pointed to 80 mg/ml concentration to obtain the most
361 pronounced effect. It was also assumed that water condensation would take place in the later
362 stage of spinning. As the humidity slows evaporation, the highest humidity allows the longest

363 time for morphology formation. The tested relative humidity Rh values were 45%, 55%, and
364 75%.

365 Fig. 11 A shows images of coatings composed of uniform polystyrenes, Fig. 11 B presents
366 images of coatings prepared from 91 kDa and 200 kDa blends, and Fig. 11 C presents images
367 of coatings prepared from 20 kDa and 200 kDa blends.

368 Each column is marked below with the mixture's PDI value, and each row corresponds to one
369 of the Rh values. Optical microscope showing three different areas of the coatings a presented
370 in the Supplementary Information, Figs. S6 – S8.

371



372

373 Fig. 11 AFM topographical images of tested samples, the colour represents the height, brighter
374 means higher. The solution concentration C was 80 mg/ml, while the samples were spun under
375 different humidity, from 0 to 75% Rh. The z-scale was chosen for the best representation of the
376 coating morphology. A – uniform coatings; B – 20 kDa and 200 kDa blends; C – 91 kDa and
377 200 kDa blends.

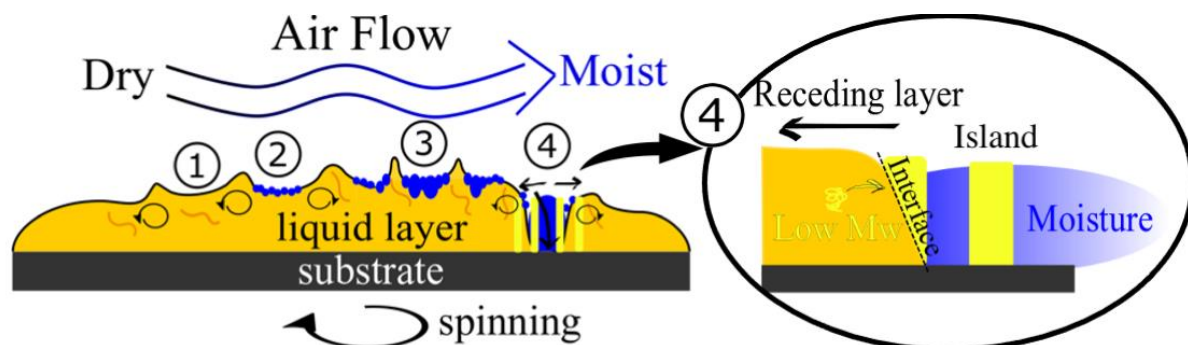
378

379 We observed that the smaller cavities (breath figures) formed around the larger cavities caused
380 by dewetting-related polymeric film ruptures. The structure that resembles the honeycomb also

381 occurred. For Rh 55%, a honeycomb-like morphology is found for all coatings, except the
382 uniform 20 kDa coating. It is hard to distinguish the uniform samples from the 90 kDa 200 kDa
383 blend. However, the 20 kDa and 200 kDa blends have distinctive morphology that depends on
384 the PDI value. Radially averaged power spectral density analysis (SI, Fig. S9) of four averaged
385 images depicts the differences between the 75/25, 50/50, and 25/75 w/w% 20 kDa and 200 kDa
386 coatings.

387 Interestingly, the coatings prepared from 20 kDa and 200 kDa bimodal blends at Rh 75% had
388 polymeric islands inside the large holes. The onset of such structures can also be observed in
389 the case of coatings prepared in Rh 55%. The fraction of the islands decreased with an increase
390 in the 200 kDa contribution. It was assumed that the islands are made of a lighter and less
391 viscous fraction. Seemingly, the heavier polymer fraction, more viscous and more entangled,
392 reinforced the honeycomb cell borders. The possible scenario is illustrated in Fig. 12. The
393 coating at Rh 0%, 45%, 55%, and 75% is marked by numbers: 1, 2, 3, 4, respectively. It is
394 assumed that the MEK did not evaporate entirely and formed MEK/20kDa and MEK/200kDa
395 fractions. It should be noticed that MEK is also soluble in water. Thus, some fraction of the
396 solvent can diffuse to the water phase. The MEK/20kDa fraction becomes dispersed in the water
397 area of the sample. The MEK/200kDa fraction forms the walls of the cells. Two explanations
398 can be proposed. First, as was shown above, the rheological properties of 200 kDa and 20kDa
399 polystyrene species differ. The more entangled 200 kDa chains act together, while the 20 kDa
400 separates from the high-tension region (higher molecular weight) towards the water/MEK
401 interface. However, water has very high polarity. Very non-polar polystyrene is forming a
402 round shape in contact. Furthermore, as was demonstrated, the solvent would deplete the 20
403 kDa fraction faster than the 200 kDa fraction, allowing for faster solidification of the 20 kDa
404 islands.

405



| Low molecular weight fraction

⌋ High molecular weight fraction

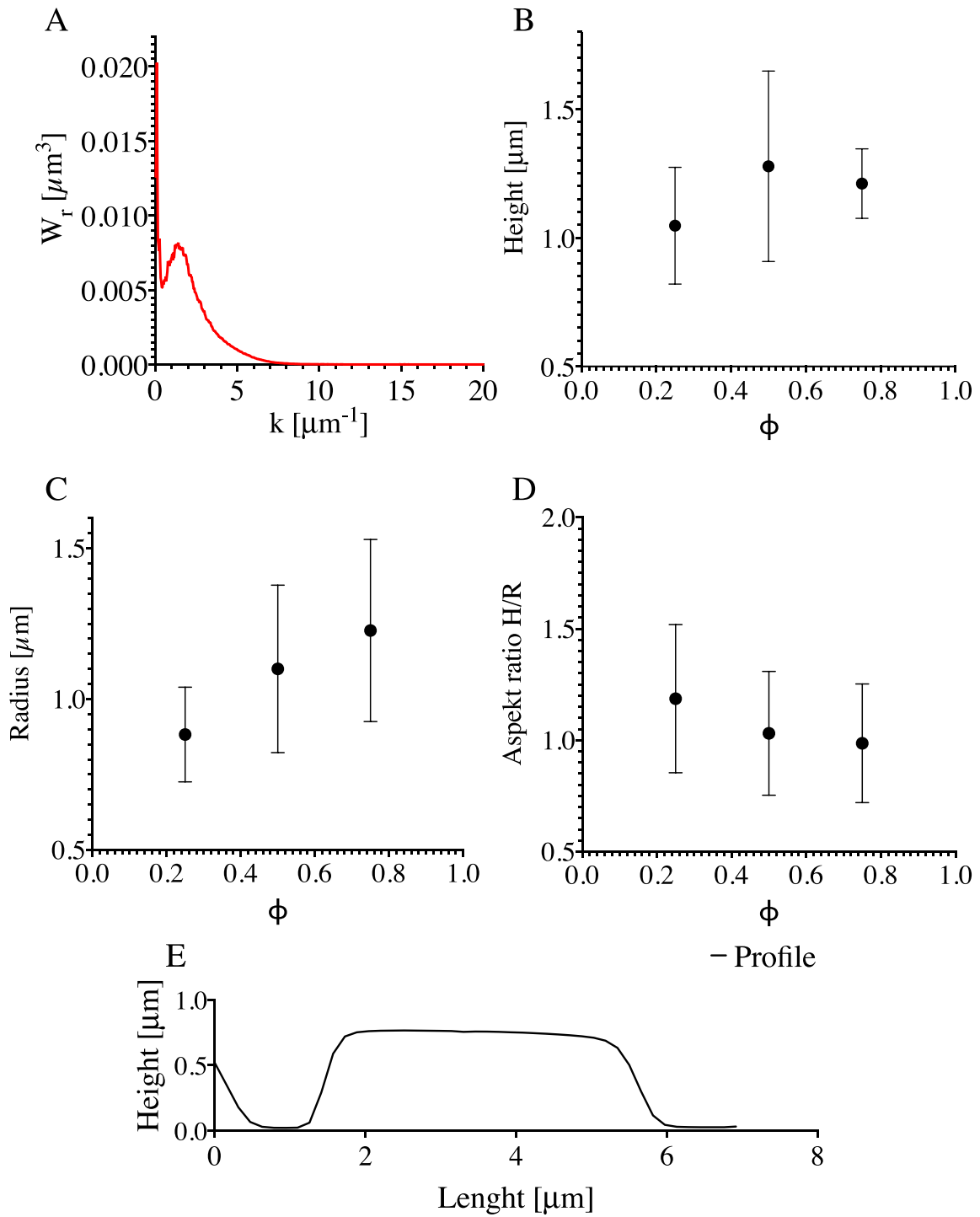
406

407 Fig. 12. Four scenarios of phase separation: spin-coating in dry air ((1), 0% Rh); moderate
 408 humidity ((2), 45% Rh; (3), 55% Rh); and high humidity ((4), 75% Rh). Low and high
 409 molecular weight fractions, convective flow driving honeycomb formation, and low molecular
 410 weight separation at the interface between the water-wetted rupture and the liquid layer of the
 411 polymer solution are presented.

412

413 Secondly, it can be discussed in terms of the two-step phase separation process discussed by
 414 Henderson et al. Their study focused on modelling the two-step quench scenario. First, the
 415 solution undergoes a temperature quench into the spinodal decomposition region. After a
 416 specific time, a secondary quench was enacted by a further decrease in the temperature. As a
 417 result, secondary domains appeared inside the already formed structures.(34) The morphology
 418 discussed there was very similar to that discussed in the current paper. The presented power
 419 spectra of the optical image of the 75/25 w/w% 20 kDa and 200 kDa coating presented in Fig.
 420 13A coincidence with the results presented in the above-mentioned paper. Nevertheless, in the
 421 current experiment, the first temperature quench is followed by the condensation of water. A
 422 decrease in temperature may facilitate the phase separation of polystyrene. Conversely, the
 423 condensation should coincide with an increase in temperature. (23) However, water may be
 424 absorbed by MEK. The MEK/water composition would be a much poorer solvent for PS. Thus,
 425 the secondary quench would occur due to the change of the solvent quality by water.

426 Fig. 13 presents the characteristic values describing the shape of the islands, Fig. 13 B – height
 427 H, Fig. 13 C - radius R, Fig. 13 D - aspect ratio H/R and Fig. 13 E – profile of an island. The
 428 dependence of the shape on the fraction of 20 kDa PS can be pointed out.



429

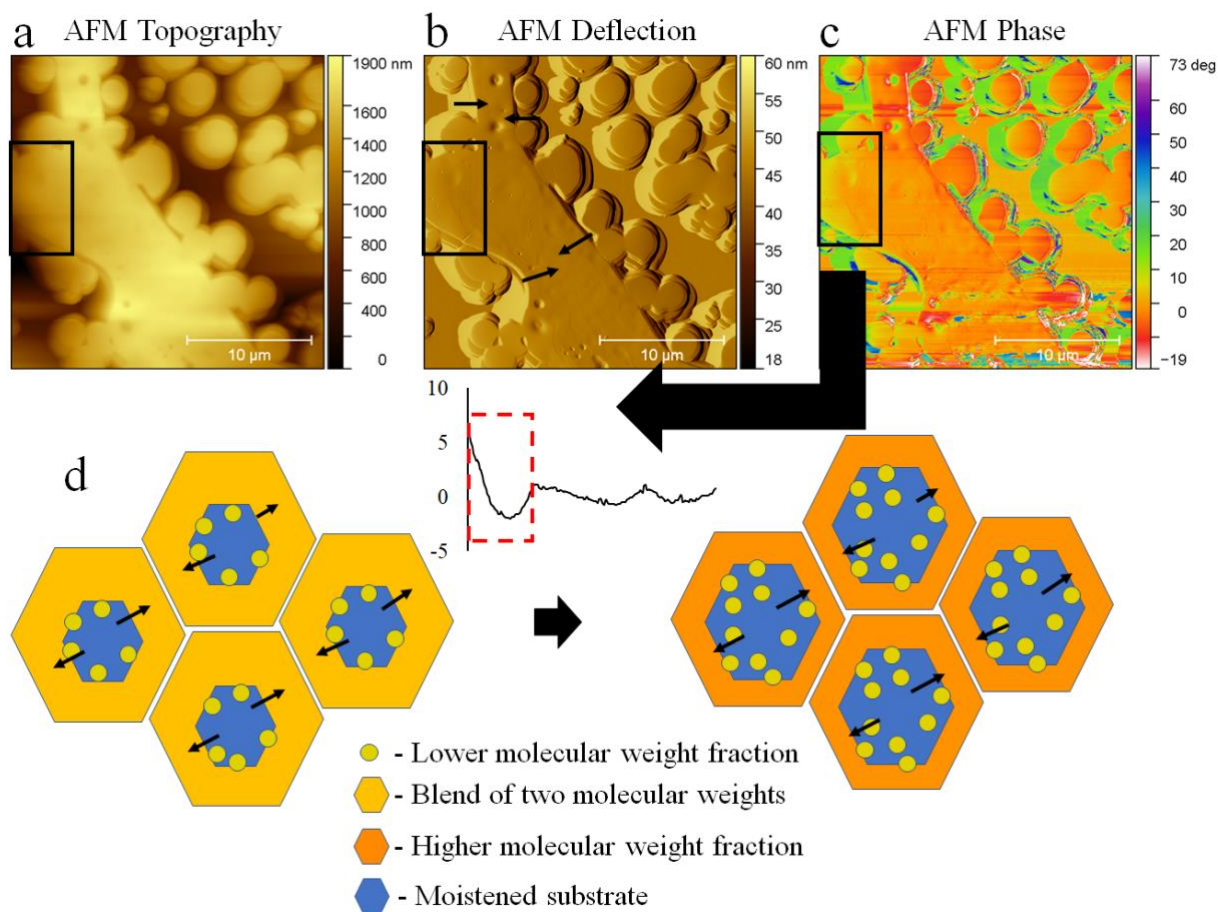
430 Fig. 13. A – Power spectra of islands/honeycomb morphology. B – Mean height, H , of islands
431 in respect to the fraction of 20 kDa PS, ϕ . C – Mean radius of islands, R . D – mean aspect ratio
432 of islands, H/R . H profile of an island.

433

434 Additionally, we tested the formation of micro islands when a short spin-coating time was used
435 (0.5 s and 1 s). These images are presented in Fig. S15 in SI. Secondary phase separation has
436 been already seen, although the islands were not fully formed.

437 The AFM image (Fig. 14 a-c) shows the event of the low molecular weight fraction separating
438 from the cell border. The cracks between the two phases and the spot where the partially formed
439 island disconnects from the bulk can be seen. The black rectangle indicates the area that differed
440 in terms of the deflection signal and phase contrast. However, the discussed phenomenon
441 appears after the thin film of the solution was formed on the substrate. The condensation needs
442 time to make holes in the films. The dewetting of the substrate by the solution can induce
443 additional motion of molecules allowing the lower molecular weight fraction to precipitate. The
444 water would also change the surface tension locally and induce the thermocapillary effects that
445 lead to the formation of convection cells (depicted in Fig 14 d).

446



447
 448 Fig. 14. AFM magnification of the cell border of the 20 kDa and 200 kDa 75/25 w/w% blend
 449 spun at Rh 75%. The black rectangle indicates the separation of different phases. The same
 450 region is shown in the form of a - topography, b - AFM deflection, the direction of dewetting
 451 is indicated by the black arrows; c - AFM phase image, an arrow indicates the phase signal
 452 difference presented as the averaged cross-section of the marked region (black box); d –
 453 schematic illustration depicting proposed formation mechanism of the honeycomb; Convection
 454 inside the liquid film led to cells formation, condensation of water led to film rupture (Blue).
 455 Subsequently, the recess of the film occurred. At the interface between the rupture area and the
 456 receding film, separation of the lower molecular fraction arises (yellow). Subsequently, the cell
 457 borders were reinforced by the remaining high molecular weight fraction (Orange);
 458

459 As mentioned, the polystyrenes used were unmodified standard grade polymers. The unchanged
460 chemical composition of the coatings was confirmed by FTIR spectroscopy (SI Fig. S10 – S12).
461 The recognized functional groups were CH₃, CH₂, and phenyl groups. These groups are
462 hydrophobic and were the driving force behind the dewetting process under high humidity
463 conditions. This argument was further reinforced by the free surface energy (SEF) measurement
464 (SI Figs. S13 – S14). The SEF of the 20 kDa coating was slightly higher than that of the 200
465 kDa coating and, consequently, led to a higher affinity for the hydrophilic SiO₂ substrate of the
466 former coating.

467

468 **Conclusions**

469 To the best of our knowledge, we have for the first time demonstrated phase separation in the
470 mixture of polystyrenes with identical chemical structure but different molecular weights. The
471 phase separation was found for 90 kDa and 200 kDa and 20 kDa and 200 kDa blends. In both
472 cases, the phase separation was found for 75/25 and 50/50 w/w% ratio. The force spectroscopy
473 was used to determine the different phases in the coatings. The phase separation was discussed
474 in terms of the difference in the viscosity of polystyrene species. Next, we have provoked
475 secondary phase separation by introducing water vapour. We have theorized that the water
476 vapour would act two-fold. The water droplets formed breath figures, and as the vapour
477 concentration increased, they caused ruptures in the liquid film. Secondly, the absorption of
478 vapour by methyl ethyl ketone, a solvent chose due to its hygroscopic properties, would
479 decrease the solubility of polystyrene. We have observed secondary phase separation for the 20
480 kDa and 200 kDa blends. But not for 90 kDa and 200 kDa blends. We also pointed out that the
481 internal thermocapillary convection and gradient of the surface tension of the top layer formed
482 convection cells inside the liquid. The ruptures caused by condensation, with the combination
483 of the convection and thermocapillary effects, formed honeycomb. The secondary phase

484 separation left the dispersed 20 kDa polystyrene phase inside the 200 kDa polystyrene
485 honeycomb.

486 The described mechanism can likely be applied to other solvent-polymer systems, consisting
487 even of three polymer fractions. It is likely possible to apply the described process to other
488 coating methods, such as dip coating, blade coating or ink-jet printing.

489

490 **Experimental**

491 • **Materials**

492 All polymers and solvents were purchased from Sigma Aldrich (Merck KGaA). One-side
493 polished ultrasmooth SiO_x wafer was purchased from Technolutions Sp. z o. o.

494

495 • **Preparation of the coatings**

496 Analytical standard grade polystyrenes (PS) obtained from the supplier with PDI = 1.04 and
497 $M_w = 20$ kDa, 91 kDa, 150 kDa, or 200 kDa were used.

498 Two kinds of blends were prepared: blends of 20 kDa and 200 kDa PS mixed in 75/25, 50/50,
499 25/75 w/w % proportions; similarly, blends of 91 kDa and 200 kDa PS were mixed in the same
500 proportions and dissolved in methyl ethyl ketone (analytic grade, MEK) and mixed for an hour
501 at 37 °C. After mixing, the solutions were stored overnight. The list of polystyrene blends used
502 is summarized in Table 1. The concentrations of these solutions ranged from 2.5 mg/ml to 80
503 mg/ml. A DIY Arduino-based spin-coater with a chamber with controlled humidity was used
504 to spin polystyrene films onto the SiO_x wafers. The experimental setup is depicted in
505 Supplementary Information (SI) Figs. S1 – S2. A 35 µl aliquot of the solution was pipetted onto
506 a 1 cm x 1 cm wafer. Spin-coating was performed in a closed chamber with a constant airflow
507 of 10 ml/min to maintain the desired humidity. The rotational speed was 2700 rpm or 3300 rpm.

508 The spinning time was set to 10 s to allow the solvent to evaporate. Solutions were spin-coated
 509 under humidity of Rh 0%, 45%, 55%, 75%.

510
 511 Table 1. List of polymer blends that were used for spin-coating.

Type of Blend	Sample code	Molecular weight M_w [kDa]		PDI
Uniform	20 kDa	20		1.04
	91 kDa	91		1.04
	150 kDa	150		1.04
	200 kDa	200		1.04
Bimodal	Sample code	Molecular weight		PDI
		$[M_w]$ [kDa] ₍₁₎	$[M_n]$ [kDa] ⁽²⁾	
91 kDa / 200 kDa	75/25*	137	118	1.16
	50/50*	166	146	1.14
	25/75*	186	173	1.08
20 kDa / 200 kDa	75/25**	158	65	2.43
	50/50**	184	110	1.67
	25/75**	194	155	1.25

512 ⁽¹⁾Weight average molecular weight $[M_w] = (f_1M_{w1}^2 + f_2M_{w2}^2)/(f_1M_{w1} + f_2M_{w2})$, ⁽²⁾Number average molecular
 513 weight $[M_n] = f_1M_{w1} + f_2M_{w2}$, where f - fraction of one of the polymers in %; PDI states for the polydispersity
 514 index.

515

516 • **Gel permeation chromatography (GPC)**

517 The number and weight average molecular weights (M_n and M_w) were determined by an Agilent
 518 1200 series GPC modular system with a refractive index detector (RID) equipped with two
 519 PLgel 5 μ m MIXED-C columns (300x7.5 mm) in the series, while the polydispersity index was
 520 calculated as the ratio of M_w/M_n . Calibration was performed using a set of 12 narrowly
 521 distributed polystyrene standards with molecular weights (M_p s) in the range of 474 g/mol - 1
 522 800 000 g/mol.

523 The measurements were performed at 35 °C. Chloroform GPC grade was used as a solvent at
 524 a flow rate of 0.7 ml/min. All samples (~2 mg/ml) were filtered through a PTFE 0.2 μ m

525 membrane before the analysis. The data were collected by ChemStation for LC and analysed
526 by ChemStation GPC Data Analysis Software.

527

528 • **Force Spectroscopy FS and Elastic Modulus**

529 When a force spectroscopy experiment is performed, an AFM probe applies strain on the film
530 surface.(67) Force spectroscopy was performed by means of atomic force microscopy (AFM,
531 Asylum Research MFP3D Bio). (68) An OMLCT-AC200TS-R3 (Olympus) cantilever was
532 used with the nominal spring constant $k = 9 \text{ N/m}$ and tip radius below 10 nm, as suggested by
533 the cantilever's producer. AFM was calibrated using the built-in thermal vibrations method.
534 The (69) Johnson, Kendall, and Roberts (JKR) model was used to calculate the elastic modulus
535 (E).(70) The indentation depth was $\sim 8 \text{ nm}$ (Supplementary Information, 4. *Force*
536 *Spectroscopy*). As we wanted to neglect the possible influence of stiff (silica) substrate on the
537 polystyrene coating's registered mechanical data, we decided to perform an FS experiment
538 using the thickest films (films spun from the solution of a concentration of 80 mg/ml).

539 Maps of a large area of the coating $80 \mu\text{m} \times 80 \mu\text{m}$ with 40×40 points were obtained. These
540 higher resolution maps are supplemented as an attachment (SI). These data were supported by
541 lower resolution maps with a resolution of 15×15 points. Each map was used to obtain the
542 mean elastic modulus value. Altogether, at least five maps were made. Ordinary one-way
543 ANOVA followed by multiple comparisons Fisher's test was used to compare different groups'
544 means.

545 Furthermore, histograms representing each higher resolution map were prepared. The skewness
546 of the elastic modulus distribution was measured. Skewness was divided into two groups: one
547 for uniform coatings and one for bimodal coatings. The t-test ($p < 0.05$) was used to compare
548 the means of these two groups.

549

550 • **Evaluation of the thickness of spin-coated films by means of atomic force**
551 **microscopy**

552 The thickness of spin-coated films was assessed based on intentionally made scratch
553 topography images (SI Fig. S3). Five randomly selected areas of each sample were tested, and
554 profiles were generated. Each of the profile lines was averaged from three contiguous lines to
555 avoid any unwanted artefacts.

556

557 • **Imaging of the coatings**

558 Inverted light microscopes (Nikon EPIPHOT 200 and Zeiss Axio Observer) were used for
559 imaging. An atomic force microscope (AFM, Asylum Research MFP3D Bio) working in
560 tapping mode (AC mode) was used to illustrate the phase composition and topography of the
561 polystyrene films.

562

563 • **In situ measurement of evaporation during spin-coating through laser light**
564 **reflectometry with stroboscopic effect**

565 In situ stroboscopic laser light reflectometry was developed to investigate the thinning of the
566 solution layer while spinning. The laser light is reflected from the coating during the spin-
567 coating process. The occurring interference pattern can be used to estimate the thinning rate of
568 the solution. (71–73) The experimental setup is described in SI, Figs. S1 – S2.

569 Depending on the thickness of the layer, constructive or destructive interference can occur. The
570 condition for the constructive interference was calculated from Bragg's law: $2n\Delta h\cos\theta = m\lambda$,
571 where n is the refractive index of the layer, Δh is the thickness of the layer, θ is the incident
572 angle, m is an integer number, and λ is the light wavelength. For pure MEK, $\Delta h = 235$ nm
573 (assuming the refractive index MEK = 1.3788). For the polymer solution, it was assumed that

574 the refractive index was $n = 1.5$; thus, $\Delta h = 217$ nm. The laser light wavelength was $\lambda = 650$
575 nm. The time resolution was 0.022 s.

576

577 • **Data analysis and visualisation**

578 For data visualization and analysis, GraphPad Prism 8 was used. Image analysis procedures
579 implemented in Gwyddion software (ver 2.50) were used.

580

581 • **Fourier Transform IR**

582 Infrared spectra were collected using a Fourier transform infrared spectrophotometer (Nicolet
583 8700 FTIR, Thermo Scientific). Measurements were performed using FTIR ATR over a range
584 of 4000–400 cm^{-1} .

585

586 • **Contact Angle and Surface Free Energy Measurement**

587 The contact angle (CA) was measured using a Data Physics OCA 20 goniometer. The contact
588 angle was measured with a sessile drop method. For surface free energy measurement (SFE),
589 two kinds of coatings were chosen: 20 kDa and 200 kDa. For each type of coating, three droplets
590 were measured, and three different coatings were used. Two liquid systems were used:
591 deionised water and diiodomethane (Sigma Aldrich, Analytic grade). The groups were
592 compared with the t-test ($p < 0.05$). The Owens, Wendt, Rabel, and Kaelble (OWKR) method
593 was used for SFE calculation. (74)

594

595 **Supporting Information (SI)**

596 Experimental setup depicting the custom-built spin-coater with a humidity-controlled chamber
597 and an in-situ interferometer with the stroboscopic effect. Illustration of thickness

598 measurement. Viscosity-related coefficients. Optical microscope images. FTIR results. Free
599 Surface Energy results.

600

601 **Author information**

602 Corresponding authors:

603 Maciej Łojkowski, ORCID: 0000-0002-0612-7964, email: 00183042@pw.edu.pl

604 Wojciech Swieszkowski, ORCID: 0000-0003-4216-9974, email:

605 wojciech.swieszkowski@pw.edu.pl.

606

607 The authors declare no competing financial interest.

608

609 **Acknowledgements**

610 This manuscript is a part of Maciej Łojkowski PhD thesis. This work was supported by
611 the National Centre for Research and Developments
612 [STRATEGMED3/306888/3/NCBR/2017]. We are grateful Mgr. Donata Kuczyńska-Zemła
613 for help with optical microscopy.

614

615 **Authors contributions:**

616 Conceptualization, M.Ł. ; methodology, M.Ł., A.Ch., E.Ch. ; investigation, M.Ł., A.Ch., E.
617 Ch., imaging, M.Ł., A.Ch. ; data analysis, M.Ł. ; visualisation, M.Ł. ; writing, M.Ł. ;
618 supervision, W. Ś.; revision of the manuscript, M.Ł., A.Ch., E. Ch., W. Ś; funding acquisition
619 W. Ś. All authors have read and agreed to the published version of the manuscript.

620

621 **Abbreviations**

622 AFM – atomic force microscopy; bimodal – polymer with two nodes in molecular weight
623 distribution; coating – final polymer coating; CA – contact angle; E – elastic modulus; film –
624 liquid film of solution spread on the substrate; FS – force spectroscopy; FTIR – Fourier
625 transform IR; GPC – gel permeation chromatography; initial solution – solution at the start of
626 spin-coating; MEK – methyl ethyl ketone; Mw – molecular weight; $[M_w]$ – weight average
627 molecular weight; $[M_n]$ – number average molecular weight; MWD – molecular weight
628 distribution; PDI – polydispersity index; PTF – polymer thin film; PS – polystyrene; Rh% -
629 relative humidity in %; RMS – root mean square roughness; uniform – polymer with one node
630 in molecular weight distribution.

631

632 **References**

- 633 1. Kumar M, Bhardwaj R. Wetting characteristics of *Colocasia esculenta* (Taro) leaf and a
634 bioinspired surface thereof. *Sci Rep.* 2020;10(1):1–15.
- 635 2. He R, Xiao J, Zhang M, Zhang Z, Zhang W, Cao Y, et al. Artificial honeycomb-
636 inspired TiO₂ nanorod arrays with tunable nano/micro interfaces for improving
637 poly(dimethylsiloxane) surface hydrophobicity. *J Mater Sci.* 2016;51(6):2935–41.
- 638 3. Jahed Z, Shahsavan H, Verma MS, Rogowski JL, Seo BB, Zhao B, et al. Bacterial
639 Networks on Hydrophobic Micropillars. *ACS Nano.* 2017;11(1):675–83.
- 640 4. Liu X, Liu R, Cao B, Ye K, Li S, Gu Y, et al. Subcellular cell geometry on micropillars
641 regulates stem cell differentiation. *Biomaterials* [Internet]. 2016 Dec;111:27–39.
642 Available from: <http://dx.doi.org/10.1016/j.biomaterials.2016.09.023>
- 643 5. Walheim S, Böltau M, Mlynek J, Krausch G, Steiner U. Structure Formation via
644 Polymer Demixing in Spin-Cast Films. *Macromolecules* [Internet]. 1997 Aug
645 1;30(17):4995–5003. Available from: <https://doi.org/10.1021/ma9619288>
- 646 6. Daly R, Sader JE, Boland JJ. The dominant role of the solvent–water interface in water

- 647 droplet templating of polymers. *Soft Matter* [Internet]. 2013;9(33):7960. Available
648 from: <http://xlink.rsc.org/?DOI=c3sm51452h>
- 649 7. Khikhlovskiy V, Wang R, van Breemen AJJM, Gelinck GH, Janssen RAJ, Kemerink
650 M. Nanoscale Organic Ferroelectric Resistive Switches. *J Phys Chem C* [Internet].
651 2014 Feb 13;118(6):3305–12. Available from:
652 <https://pubs.acs.org/doi/10.1021/jp409757m>
- 653 8. D'Andrade BW, Forrest SR. White Organic Light-Emitting Devices for Solid-State
654 Lighting. *Adv Mater* [Internet]. 2004 Sep 16;16(18):1585–95. Available from:
655 <http://doi.wiley.com/10.1002/adma.200400684>
- 656 9. Yabu H. Fabrication of honeycomb films by the breath figure technique and their
657 applications. *Sci Technol Adv Mater* [Internet]. 2018;19(1):802–22. Available from:
658 <https://doi.org/10.1080/14686996.2018.1528478>
- 659 10. Wu D, Xu F, Sun B, Fu R, He H, Matyjaszewski K. Design and Preparation of Porous
660 Polymers. *Chem Rev* [Internet]. 2012 Jul 11;112(7):3959–4015. Available from:
661 <https://pubs.acs.org/doi/10.1021/cr200440z>
- 662 11. Karagkiozaki V, Vavoulidis E, Karagiannidis PG, Gioti M, Fatouros DG, Vizirianakis
663 IS, et al. Development of a nanoporous and multilayer drug-delivery platform for
664 medical implants. *Int J Nanomedicine*. 2012;7(October):5327–38.
- 665 12. Calejo MT, Ilmarinen T, Skottman H, Kellomäki M. Breath figures in tissue
666 engineering and drug delivery: State-of-the-art and future perspectives. Vol. 66, *Acta*
667 *Biomaterialia*. 2018.
- 668 13. Vendra VK, Wu L, Krishnan S. Polymer Thin Films for Biomedical Applications. In:
669 *Nanotechnologies for the Life Sciences* [Internet]. Weinheim, Germany: Wiley-VCH
670 Verlag GmbH & Co. KGaA; 2011. Available from:
671 <http://doi.wiley.com/10.1002/9783527610419.ntls0179>

- 672 14. Griesser HJ. *Thin Film Coatings for Biomaterials and Biomedical Applications*, 1st
673 Edition. 2016. 310 p.
- 674 15. Łojkowski M, Walheim S, Jokubauskas P, Schimmel T, Świążkowski W. Tuning the
675 wettability of a thin polymer film by gradually changing the geometry of nanoscale
676 pore edges. *Langmuir* [Internet]. 2019;35(17):5987–96. Available from:
677 <https://doi.org/10.1021/acs.langmuir.9b00467>
- 678 16. Plawsky JL, Kim JK, Schubert EF. Engineered nanoporous and nanostructured films.
679 *Mater Today* [Internet]. 2009;12(6):36–45. Available from:
680 [http://dx.doi.org/10.1016/S1369-7021\(09\)70179-8](http://dx.doi.org/10.1016/S1369-7021(09)70179-8)
- 681 17. Bormashenko E. Breath-figure self-assembly, a versatile method of manufacturing
682 membranes and porous structures: Physical, chemical and technological aspects.
683 *Membranes* (Basel). 2017;7(3).
- 684 18. Birnie DP. Rational solvent selection strategies to combat striation formation during
685 spin coating of thin films. *J Mater Res*. 2001;16(4):1145–54.
- 686 19. van Franeker JJ, Westhoff D, Turbiez M, Wienk MM, Schmidt V, Janssen RAJ.
687 Controlling the Dominant Length Scale of Liquid-Liquid Phase Separation in Spin-
688 coated Organic Semiconductor Films. *Adv Funct Mater* [Internet]. 2015
689 Feb;25(6):855–63. Available from: <http://doi.wiley.com/10.1002/adfm.201403392>
- 690 20. Schaefer C, Michels JJ, van der Schoot P. Structuring of Thin-Film Polymer Mixtures
691 upon Solvent Evaporation. *Macromolecules* [Internet]. 2016 Sep 27;49(18):6858–70.
692 Available from: <https://pubs.acs.org/doi/10.1021/acs.macromol.6b00537>
- 693 21. Ebbens S, Hodgkinson R, Parnell AJ, Dunbar A, Martin SJ, Topham PD, et al. In Situ
694 Imaging and Height Reconstruction of Phase Separation Processes in Polymer Blends
695 during Spin Coating. *ACS Nano* [Internet]. 2011 Jun 28;5(6):5124–31. Available from:
696 <https://pubs.acs.org/doi/10.1021/nn201210e>

- 697 22. Danglad-Flores J, Eickelmann S, Riegler H. Deposition of polymer films by spin
698 casting: A quantitative analysis. *Chem Eng Sci* [Internet]. 2018 Apr;179:257–64.
699 Available from: <https://linkinghub.elsevier.com/retrieve/pii/S0009250918300125>
- 700 23. Dombrovsky LA, Frenkel M, Legchenkova I, Bormashenko E. Effect of thermal
701 properties of a substrate on formation of self-arranged surface structures on evaporated
702 polymer films. *Int J Heat Mass Transf* [Internet]. 2020;158:120053. Available from:
703 <https://doi.org/10.1016/j.ijheatmasstransfer.2020.120053>
- 704 24. Daly R, Sader JE, Boland JJ. Taming Self-Organization Dynamics to Dramatically
705 Control Porous Architectures. *ACS Nano* [Internet]. 2016 Mar 22;10(3):3087–92.
706 Available from: <https://pubs.acs.org/doi/10.1021/acsnano.5b06082>
- 707 25. Zabusky HH, Heitmiller RF. Properties of high density polyethylenes with bimodal
708 molecular weight distribution. *Polym Eng Sci*. 1964;4(1):17–21.
- 709 26. Wu BH, Zhong QZ, Xu ZK, Wan LS. Effects of molecular weight distribution on the
710 self-assembly of end-functionalized polystyrenes. *Polym Chem*. 2017;8(29):4290–8.
- 711 27. Jiang H, Zhang L, Qin J, Zhang W, Cheng Z, Zhu X. Producing bimodal molecular
712 weight distribution polymers through facile one-pot/one-step RAFT polymerization. *J*
713 *Polym Sci Part A Polym Chem*. 2012;50(19):4103–9.
- 714 28. Whitfield R, Parkatzidis K, Truong NP, Junkers T, Anastasaki A. Tailoring Polymer
715 Dispersity by RAFT Polymerization: A Versatile Approach. *Chem* [Internet]. 2020
716 Jun;6(6):1340–52. Available from:
717 <https://linkinghub.elsevier.com/retrieve/pii/S2451929420301923>
- 718 29. Tanaka K, Takahara A, Kajiyama T. Effect of Polydispersity on Surface Molecular
719 Motion of Polystyrene Films. *Macromolecules* [Internet]. 1997 Oct;30(21):6626–32.
720 Available from: <https://pubs.acs.org/doi/10.1021/ma970057e>
- 721 30. Heitmiller RF, Naar RZ, Zabusky HH. Effect of homogeneity on viscosity in capillary

- 722 extrusion of polyethylene. *J Appl Polym Sci* [Internet]. 1964 Mar;8(2):873–80.
723 Available from: <http://doi.wiley.com/10.1002/app.1964.070080226>
- 724 31. Koningsveld R, Chermin HAG, Gordon M. Liquid–liquid phase separation in
725 multicomponent polymer solutions - VIII. Stability limits and consolute states in quasi-
726 ternary mixtures. *Proc R Soc London A Math Phys Sci* [Internet]. 1970 Oct
727 27;319(1538):331–49. Available from:
728 <https://royalsocietypublishing.org/doi/10.1098/rspa.1970.0182>
- 729 32. Zeman L, Patterson D. Effect of the Solvent on Polymer Incompatibility in Solution.
730 *Macromolecules* [Internet]. 1972 Jul;5(4):513–6. Available from:
731 <https://pubs.acs.org/doi/abs/10.1021/ma60028a030>
- 732 33. Shultz AR, Flory PJ. Phase Equilibria in Polymer—Solvent Systems 1,2. *J Am Chem*
733 *Soc* [Internet]. 1952 Oct 1;74(19):4760–7. Available from:
734 <https://doi.org/10.1021/ja01139a010>
- 735 34. Henderson IC, Clarke N. Two-Step Phase Separation in Polymer Blends.
736 *Macromolecules*. 2004;37(5):1952–9.
- 737 35. Tanaka H. Viscoelastic phase separation in soft matter and foods. *Faraday Discuss*.
738 2012;158:371–406.
- 739 36. Hengeller L, Huang Q, Dorokhin A, Alvarez NJ, Almdal K, Hassager O. Stress
740 relaxation of bi-disperse polystyrene melts: Exploring the interactions between long
741 and short chains in non-linear rheology. *Rheol Acta*. 2016;55(4):303–14.
- 742 37. Harris EK. Effect of blending on the rheological properties of polystyrene. *J Appl*
743 *Polym Sci* [Internet]. 1973 Jun;17(6):1679–92. Available from:
744 <http://doi.wiley.com/10.1002/app.1973.070170604>
- 745 38. Klein J. The Onset of Entangled Behavior in Semidilute and Concentrated Polymer
746 Solutions. *Macromolecules* [Internet]. 1978 Sep;11(5):852–8. Available from:

- 747 <https://pubs.acs.org/doi/abs/10.1021/ma60065a002>
- 748 39. Hong KM, Noolandi J. Theory of inhomogeneous multicomponent polymer systems.
749 Macromolecules [Internet]. 1981 May;14(3):727–36. Available from:
750 <https://pubs.acs.org/doi/abs/10.1021/ma50004a051>
- 751 40. Hariharan A, Kumar SK, Russell TP. A lattice model for the surface segregation of
752 polymer chains due to molecular weight effects. Macromolecules [Internet]. 1990
753 Jul;23(15):3584–92. Available from:
754 <https://pubs.acs.org/doi/abs/10.1021/ma00217a009>
- 755 41. Mahmoudi P, Matsen MW. Entropic segregation of short polymers to the surface of a
756 polydisperse melt. Eur Phys J E [Internet]. 2017 Oct 6;40(10):85. Available from:
757 <http://link.springer.com/10.1140/epje/i2017-11575-7>
- 758 42. Hill JA, Endres KJ, Mahmoudi P, Matsen MW, Wesdemiotis C, Foster MD. Detection
759 of Surface Enrichment Driven by Molecular Weight Disparity in Virtually
760 Monodisperse Polymers. ACS Macro Lett [Internet]. 2018 Apr 17;7(4):487–92.
761 Available from: <https://pubs.acs.org/doi/10.1021/acsmacrolett.7b00993>
- 762 43. Stein GE, Laws TS, Verduzco R. Tailoring the Attraction of Polymers toward Surfaces.
763 Macromolecules [Internet]. 2019 Jul 9;52(13):4787–802. Available from:
764 <https://pubs.acs.org/doi/10.1021/acs.macromol.9b00492>
- 765 44. Carlier V, Sclavons M, Jonas AM, Jérôme R, Legras R. Probing Thermoplastic
766 Matrix–Carbon Fiber Interphases. 1. Preferential Segregation of Low Molar Mass
767 Chains to the Interface. Macromolecules [Internet]. 2001 May;34(11):3725–9.
768 Available from: <https://pubs.acs.org/doi/10.1021/ma000404b>
- 769 45. Suwa J, Kakiage M, Yamanobe T, Komoto T, Uehara H. Molecular Weight
770 Segregation on Surfaces of Polyethylene Blended Films as Estimated from
771 Nanoscratch Tests Using Scanning Probe Microscopy. Langmuir [Internet]. 2007

- 772 May;23(11):5882–5. Available from: <https://pubs.acs.org/doi/10.1021/la070150o>
- 773 46. Karim A, Slawecki TM, Kumar SK, Douglas JF, Satija SK, Han CC, et al. Phase-
774 Separation-Induced Surface Patterns in Thin Polymer Blend Films. *Macromolecules*
775 [Internet]. 1998 Feb;31(3):857–62. Available from:
776 <https://pubs.acs.org/doi/10.1021/ma970687g>
- 777 47. Hoppe H, Heuberger M, Klein J. Self-Similarity and Pattern Selection in the
778 Roughening of Binary Liquid Films. *Phys Rev Lett* [Internet]. 2001 May
779 21;86(21):4863–6. Available from:
780 <https://link.aps.org/doi/10.1103/PhysRevLett.86.4863>
- 781 48. Heier J, Kramer EJ, Revesz P, Battistig G, Bates FS. Spinodal Decomposition in a
782 Subsurface Layer of a Polymer Blend Film. *Macromolecules* [Internet]. 1999
783 Jun;32(11):3758–65. Available from: <https://pubs.acs.org/doi/10.1021/ma981709h>
- 784 49. Jandt KD, Heier J, Bates FS, Kramer EJ. Transient surface roughening of thin films of
785 phase separating polymer mixtures. *Langmuir*. 1996;12(15):3716–20.
- 786 50. Huang C, Förste A, Walheim S, Schimmel T. Polymer blend lithography for metal
787 films: Large-area patterning with over 1 billion holes/inch². *Beilstein J Nanotechnol*.
788 2015;6(1):1205–11.
- 789 51. Flory PJ, Höcker H. Thermodynamics of polystyrene solutions. Part 1.—Polystyrene
790 and methyl ethyl ketone. *Trans Faraday Soc* [Internet]. 1971;67:2258–69. Available
791 from: <http://xlink.rsc.org/?DOI=TF9716702258>
- 792 52. Imre A, Van Hook WA. Liquid-liquid demixing from solutions of polystyrene. 1. A
793 review. 2. Improved correlation with solvent properties. Vol. 25, *Journal of Physical*
794 *and Chemical Reference Data*. 1996. p. 637–61.
- 795 53. Utracki LA, Wilkie CA. Polymer blends handbook. *Polymer Blends Handbook*. 2014.
796 1–2378 p.

- 797 54. Ying Q, Chu B. Overlap concentration of macromolecules in solution. *Macromolecules*
798 [Internet]. 1987 Mar;20(2):362–6. Available from:
799 <https://pubs.acs.org/doi/abs/10.1021/ma00168a023>
- 800 55. Kim JK, Taki K, Nagamine S, Ohshima M. Periodic porous stripe patterning in a
801 polymer blend film induced by phase separation during spin-casting. *Langmuir*.
802 2008;24(16):8898–903.
- 803 56. Heier J, Kramer EJ, Groenewold J, Fredrickson GH. Kinetics of individual block
804 copolymer island formation and disappearance near an absorbing boundary.
805 *Macromolecules*. 2000;33(16):6060–7.
- 806 57. Coveney S, Clarke N. Pattern formation in polymer blend thin films: Surface
807 roughening couples to phase separation. *Phys Rev Lett*. 2014;113(21):1–5.
- 808 58. Mecke K. Additivity, Convexity, and Beyond: Applications of Minkowski Functionals
809 in Statistical Physics. *Stat Phys Spat Stat* [Internet]. 2000;111–84. Available from:
810 http://link.springer.com/chapter/10.1007/3-540-45043-2_6
- 811 59. Wolf BA. Improvement of polymer solubility: Influence of shear and of pressure. *Pure*
812 *Appl Chem*. 1997;69(5):929–33.
- 813 60. Du B, Tsui OKC, Zhang Q, He T. Study of Elastic Modulus and Yield Strength of
814 Polymer Thin Films Using Atomic Force Microscopy. *Langmuir* [Internet]. 2001
815 May;17(11):3286–91. Available from: <https://pubs.acs.org/doi/10.1021/la001434a>
- 816 61. Landel RF, Nielsen LE. *Mechanical properties of polymers and composites*. CRC
817 press; 1993.
- 818 62. Torres JM, Stafford CM, Vogt BD. Impact of molecular mass on the elastic modulus of
819 thin polystyrene films. *Polymer (Guildf)* [Internet]. 2010;51(18):4211–7. Available
820 from: <http://dx.doi.org/10.1016/j.polymer.2010.07.003>
- 821 63. Kok CM, Rudin A. Prediction of Flory–Huggins interaction parameters from intrinsic

- 822 viscosities. *J Appl Polym Sci*. 1982;27(2):353–62.
- 823 64. Lee SH, Lee SB. The Hildebrand solubility parameters, cohesive energy densities and
824 internal energies of 1-alkyl-3-methylimidazolium-based room temperature ionic
825 liquids. *Chem Commun*. 2005;(27):3469–71.
- 826 65. Bormashenko E, Malkin A, Musin A, Bormashenko Y, Whyman G, Litvak N, et al.
827 Mesoscopic patterning in evaporated polymer solutions: Poly(ethylene glycol) and
828 room-temperature-vulcanized polyorganosilanes/-siloxanes promote formation of
829 honeycomb structures. *Macromol Chem Phys*. 2008;209(6):567–76.
- 830 66. Uchiyama H, Matsui T, Kozuka H. Spontaneous Pattern Formation Induced by
831 Bénard–Marangoni Convection for Sol–Gel-Derived Titania Dip-Coating Films: Effect
832 of Co-solvents with a High Surface Tension and Low Volatility. *Langmuir* [Internet].
833 2015 Nov 17;31(45):12497–504. Available from:
834 <https://pubs.acs.org/doi/10.1021/acs.langmuir.5b02929>
- 835 67. Zgłobicka I, Chlanda A, Woźniak M, Łojkowski M, Szoszkiewicz R, Mazurkiewicz-
836 Pawlicka M, et al. Microstructure and nanomechanical properties of single stalks from
837 diatom *Didymosphenia geminata* and their change due to adsorption of selected metal
838 ions. *J Phycol*. 2017;53(4).
- 839 68. Chlanda A, Kijeńska-Gawrońska E, Zdunek J, Swieszkowski W. Internal
840 nanocrystalline structure and stiffness alterations of electrospun polycaprolactone-
841 based mats after six months of in vitro degradation. An atomic force microscopy assay.
842 *J Mech Behav Biomed Mater* [Internet]. 2020 Jan;101(August 2019):103437.
843 Available from: <https://linkinghub.elsevier.com/retrieve/pii/S1751616119305156>
- 844 69. Sader JE, Borgani R, Gibson CT, Haviland DB, Michael J, Kilpatrick JI, et al. A virtual
845 instrument to standardise the calibration of atomic force microscope cantilevers. *Rev*
846 *Sci Instrum* [Internet]. 2016 Sep 1;87(9):093711. Available from:

847 <http://dx.doi.org/10.1063/1.4962866>

- 848 70. Wu KC, You HI. Determination of solid material elastic modulus and surface energy
849 based on JKR contact model. *Appl Surf Sci.* 2007;253(20):8530–7.
- 850 71. Toolan DTW. Straightforward technique for in situ imaging of spin-coated thin films .
851 *Opt Eng.* 2015;54(2):024109.
- 852 72. Toolan DTW, Howse JR. Development of in situ studies of spin coated polymer films.
853 *J Mater Chem C.* 2013;1(4):603–16.
- 854 73. Mokarian-Tabari P, Geoghegan M, Howse JR, Heriot SY, Thompson RL, Jones RAL.
855 Quantitative evaluation of evaporation rate during spin-coating of polymer blend films:
856 Control of film structure through defined-atmosphere solvent-casting. *Eur Phys J E.*
857 2010;33(4):283–9.
- 858 74. Drelich JW, Boinovich L, Chibowski E, Volpe C Della, Hołysz L, Marmur A, et al.
859 Contact Angles: History of Over 200 Years of Open Questions. *Surf Innov* [Internet].
860 2019;(March):1–25. Available from:
861 <https://www.icevirtuallibrary.com/doi/10.1680/jsuin.19.00007>

862

863 Fig 1. Exemplary GPC experiment results of bimodal and uniform MWD polystyrene; A -
864 narrow uniform MWD, $M_w = 91$ kDa, PDI 1.04; B – bimodal MWD, blend of $M_w = 91$ kDa,
865 PDI = 1.04 and $M_w = 200$ kDa, PDI = 1.04.

866

867 Fig. 2. Reduced viscosity η_r/C of the solutions, A - η_r/C plotted against the solution's
868 concentration. Curves represent fits for eq. 2; B - η_r/C plotted as a function of the number
869 average molecular weight function. Curves represent the Mark-Houwink equation fit (eq. 3),
870 $[M_n] = f_1M_{w1} + f_2M_{w2}$, where f is w/w % ratio of polymers.

871

872 Fig. 3. The relation between the evaporation rate of solution and the reduced viscosity of
873 solution for polymer concentrations: A - 20 mg/ml, B - 40 mg/ml, and C - 80 mg/ml. The curves
874 represent the Padé approximation trend-line.

875

876 Fig. 4. A - Thickness of the coatings with respect to the composition and the concentration. The
877 plot presents data for uniform and 91 kDa/200 kDa solutions. B – Thickness of the coating for
878 80 mg/ml concentration in the blend's molecular weight function. * - Blends of 91 kDa and 200
879 kDa polystyrene; ** - blend of 20 kDa and 200 kDa polystyrene; x/x – w/w% ratio of blended
880 homogeneous polystyrenes. The number average molecular weight $[M_n] = f_1M_{w1} + f_2M_{w2}$,
881 where f w/w. % ratio of polymers. C - RMS roughness of the coatings spun from 80 mg/ml
882 concentration.

883

884 Fig. 5. A - Optical images of coatings spun from 80 mg/ml. The B - Minkowski connectivity
885 $C(\nu)$ of the coatings spun from 80 mg/ml, where ν represents the threshold for the image
886 binarization; The values on the axis were normalized to 1.

887

888 Fig. 6. Average elastic modulus obtained based on the FS method for coatings made from a
889 solution of 80 mg/ml. Uniform – coatings were made from homogeneous solutions; bimodal –
890 coatings made from solutions with bimodal MWD; * - blends of 91 kDa and 200 kDa
891 polystyrene; ** - blend of 20 kDa and 200 kDa polystyrene; x/x – w/w% ratio of blended
892 homogeneous polystyrenes. $[M_n] = f_1M_{w1} + f_2M_{w2}$, where f w/w % ratio of polymers. *** -
893 means are significantly different (one-way ANOVA, $p < 0.05$).

894

895 Fig. 7. Force Spectroscopy maps of bimodal MWD coatings and corresponding histograms of
896 the elastic modulus. The greyscale shows the stiffness – the white colour corresponds to the
897 highest stiffness. The grayscale range is ± 1 GPa.

898

899 Fig. 8. Force spectroscopy maps of coatings with uniform MWD and corresponding histograms
900 of the elastic modulus. The greyscale shows the stiffness – the white colour corresponds to the
901 highest stiffness. The grayscale range is ± 1 GPa.

902

903 Fig 9. The skewness of the elastic modulus data sets. Uniform – grouped means that represents
904 the skewness of histograms of uniform coatings elastic modulus. Bimodal – grouped means that
905 represents the skewness of histograms of all kinds of bimodal blends elastic modulus. The
906 means of these two groups were significantly different ($p < 0.05$).

907

908 Fig. 10. The effective miscibility parameter δ_{eff} of the polystyrenes in MEK with bimodal and
909 uniform distributions for two kinds of bimodal distributions: 20 kDa/200 kDa – brown squares
910 and 91 kDa/200 kDa – purple triangles; the blue circles represent data for polystyrenes with
911 uniform distributions. $[M_n] = f_1M_{w1} + f_2M_{w2}$, where f w/w % ratio of polymers.

912

913 Fig. 11 AFM topographical images of tested samples, the colour represents the height, brighter
914 means higher. The solution concentration C was 80 mg/ml, while the samples were spun under
915 different humidity, from 0 to 75% Rh. The z-scale was chosen for the best representation of the
916 coating morphology. A – uniform coatings; B – 20 kDa and 200 kDa blends; C – 91 kDa and
917 200 kDa blends.

918

919 Fig. 12. Four scenarios of phase segregation: spin-coating in dry air ((1), 0% Rh); moderate
920 humidity ((2), 45% Rh; (3), 55% Rh); and high humidity ((4), 75% Rh). Low and high
921 molecular weight fractions, convective flow driving honeycomb formation, and low molecular
922 weight separation at the interface between the water-wetted rupture and the liquid layer of the
923 polymer solution are presented.

924

925 Fig. 13. A – Power spectra of islands/honeycomb morphology. B – Mean height, H , of islands
926 in respect to the fraction of 20 kDa PS, ϕ . C – Mean radius of islands, R . D – mean aspect ratio
927 of islands, H/R . H profile of an island.

928

929 Fig. 14. AFM magnification of the cell border of the 20 kDa and 200 kDa 75/25 w/w% blend
930 spun at Rh 75%. The black rectangle indicates the separation of different phases. The same
931 region is shown in the form of a - topography, b - AFM deflection, the direction of dewetting
932 is indicated by the black arrows; c - AFM phase image, an arrow indicates the phase signal
933 difference presented as the averaged cross-section of the marked region (black box); d –
934 schematic illustration depicting proposed formation mechanism of the honeycomb; Convection
935 inside the liquid film led to cells formation, condensation of water led to film rupture (Blue).
936 Subsequently, the recess of the film occurred. At the interface between the rupture area and the
937 receding film, segregation of the lower molecular fraction arises (yellow). Subsequently, the
938 cell borders were reinforced by the remaining high molecular weight fraction (Orange);

939